

INVESTIGATION OF FRACTURE TOUGHNESS OF LAMINATED STITCHED  
COMPOSITES



LD 1780  
By  
LEISHAN CHEN

A DISSERTATION PRESENTED TO THE GRADUATE SCHOOL  
OF THE UNIVERSITY OF FLORIDA IN PARTIAL FULFILLMENT  
OF THE REQUIREMENTS FOR THE DEGREE OF  
DOCTOR OF PHILOSOPHY

UNIVERSITY OF FLORIDA

2002

To my wife Dan Xie, my son Rui Chen  
my parents Decun Chen and Shanyue Meng  
my sisters Xiaolan Chen and Lirong Chen

## ACKNOWLEDGMENTS

I would like to express my sincere gratitude to my advisors, Dr. Peter G. Ifju and Dr. Bhavani V. Sankar, for their patient guidance, constant encouragement, endless support and constructive criticism during my study.

Dr. Peter G. Ifju guided me to the wonderful experimental world with which I had little experience before. His rich knowledge, creative thinking, understanding, curiosity, positive attitude and witty character are examples I have been following for my life. Dr. Bhavani V. Sankar steered me to the composite field. His profound knowledge and deep understanding of materials and structures set a high bar for me to reach in the future.

Special thanks are owed to Dr. Nicolae D. Cristescu, Dr. David A. Jenkins and Dr. Gary R. Consolazio for serving as my supervisory committee members and for giving me wonderful ideas and advice.

Finally, I am grateful to my wife Dan Xie, my son Rui Chen, my parents Decun Chen and Shanyue Meng, and my sisters Xiaolan Chen and Lirong Chen for their love, support and encouragement.

## TABLE OF CONTENTS

	<u>page</u>
ACKNOWLEDGMENTS .....	iii
LIST OF TABLES .....	vi
LIST OF FIGURES .....	vii
ABSTRACT .....	xi
 CHAPTERS	
1 BACKGROUND AND LITERATURE SURVEY .....	1
1.1 Background .....	1
1.2 Literature Survey .....	4
2 PRELIMINARY MODE I TEST AND ANALYSIS .....	14
2.1 Introduction .....	15
2.2 Modified DCB Test .....	17
2.2.1 New Fixture .....	17
2.2.2 Specimen Preparation .....	18
2.2.3 Fixture Verification .....	18
2.2.4 Testing of Stitched Specimens .....	19
2.3 Analysis .....	21
2.3.1 Governing Equations .....	21
2.3.2 Verification of the Model .....	23
2.3.3 Instantaneous $G_{IC}$ .....	23
2.4 Conclusions .....	24
3 FINAL DESIGN OF MODE I TEST FIXTURE .....	36
3.1 Description of the New Test Fixture .....	37
3.2 Analysis of the Specimen .....	38
3.3 Results and Discussion .....	42
3.4 Conclusion .....	44
4 MODE II FRACTURE TOUGHNESS OF STITCHED COMPOSITES .....	59
4.1 Introduction .....	59

4.2 End-Notched Flexure Test .....	60
4.2.1 Three-Point Bending Setup .....	61
4.2.2 Cantilever Beam Setup .....	61
4.3 Methods of Analysis and Results .....	62
4.3.1 Average Strain Energy Release Rate Using Area Method .....	63
4.3.2 Determine the Stress Intensity Factor by Using High Sensitivity Moire Interferometry Technique .....	64
4.3.2.1 Stress intensity factor for orthotropic brittle materials ...	65
4.3.2.2 Results from moire fringe patterns of both setups .....	67
4.4 Stress Intensity Factor $K_{II\text{-parent}}$ and $K_{II\text{-eff}}$ and Strain Energy Release Rate $G_{II\text{-parent}}$ and $G_{II\text{-eff}}$ .....	68
4.5 Conclusions .....	71
5 NEW MIXED MODE TEST SETUPS .....	87
5.1 Introduction .....	88
5.2 Test Procedures .....	88
5.2.1 Novel Setup I .....	89
5.2.2 Novel Setup II .....	90
5.2.3 Novel Setup III .....	91
5.3 Results and Discussion .....	92
5.4 Conclusion .....	93
6 FINITE ELEMETN ANALYSIS .....	107
6.1 Finite Element Analysis for Mode I .....	108
6.1.1 Specimen .....	108
6.1.2 Effective Modulus $E_f$ .....	109
6.1.3 J-integral, "parent G" and "effective G" .....	110
6.1.4 2D Solid Modeling .....	112
6.1.4.1 Procedure of modeling .....	112
6.1.4.2 Results from 2D solid model .....	114
6.1.5 2D Shell Element Modeling .....	115
6.1.5.1 Modeling procedure .....	115
6.1.5.2 Results and discussion .....	116
6.1.6 Three Dimensional Model .....	117
6.1.7 Diameter vs. Density of Stitches .....	119
6.2 Finite Element Model of Mode II .....	121
6.2.1 Modeling Procedure .....	121
6.2.2 Results and Discussion .....	123
7 SUMMARY AND DISCUSSION .....	145
REFERENCES .....	149
BIOGRAPHICAL SKETCH .....	155

## LIST OF TABLES

<u>Table</u>	<u>page</u>
2-1 Comparison between two methods .....	19
5-1 Mixed mode strain energy release rate of various ratio of Mode I and Mode II .....	92
6-1 One stack of materials .....	108
6-2 Material properties .....	109
6-3 Input data from the experiment and analysis .....	113
6-4 Values of $G_{I\text{-parent}}$ and $G_{I\text{-eff}}$ under various loads .....	115
6-5 Material properties for shell elements .....	116
6-6 Comparison of $G_{I\text{-parent}}$ and $G_{I\text{-eff}}$ between two models .....	119
6-7 $G_{I\text{-eff}}$ under two simulations .....	120
6-8 Loads and crack lengths of Mode II test .....	122
6-9 Comparison of $G_{II\text{-parent}}$ and $G_{II\text{-eff}}$ under different loading conditions ....	123

## LIST OF FIGURES

<u>Figure</u>	<u>page</u>
1-1 Two types of translaminar reinforcement: continuous (Stitching) and discontinuous (Z-pinning) .....	12
1-2 Types of stitches: (A) lock stitch, (B) modified lock stitch, and (C) chain stitch .....	13
2-1 Standard DCB test method .....	26
2-2 Standard DCB test for high density stitched composites .....	27
2-3 Aluminum tabs bonded over entire specimen .....	28
2-4 Modified DCB test .....	29
2-5 Progressive loading of the preliminary fixture .....	30
2-6 Axial displacement vs. load, crack extension and opening .....	31
2-7 Crack extension vs. opening .....	32
2-8 Load vs. axial displacement under two crack lengths – $a$ and $a'$ .....	33
2-9 Critical strain energy release rate vs. load .....	34
2-10 Critical strain energy release rate ( $G_{IC}$ ) vs. crack length .....	35
3-1 New DCB test setup .....	46
3-2 Notches in the specimen .....	47
3-3 Schematic of the specimen grips. Note that the specimen grips match the notches in the specimen shown in Fig. 3.2 .....	48
3-4 View of the assembled specimen .....	49
3-5 Series of pictures taken during the new DCB test .....	50

3-6	Schematic of the new DCB test setup and free body diagram of portion AB of a specimen .....	51
3-7	Load vs. displacement for a DCB specimen -- the twenty peak loads match twenty rows of broken stitches .....	52
3-8	Bending moment distribution along one arm of the DCB specimen for a crack length of 44.2 mm and load of 5420 N .....	53
3-9	Deflection curve of one arm of the DCB specimen at a load of 5420 N and crack length of 44.2 mm .....	54
3-10	Slope vs. distance from the crack tip for crack length=44.2 mm and load=5420 N .....	55
3-11	Crack-tip bending moment variation as the crack propagates. Results for three specimens are shown .....	56
3-12	Crack-tip shear forces vs. crack length for three specimens .....	57
3-13	Instantaneous $G_{IC}$ of three specimens as a function of crack length ...	58
4-1	Three point bending for end notched flexure test setup .....	73
4-2	Schematic of the cantilever beam setup .....	74
4-3	Moiré interferometry fringe patterns on the edge of an ENF specimen	75
4-4	Load vs. displacement diagram of the three point bending setup .....	76
4-5	Load vs. displacement diagram of the cantilever beam setup .....	77
4-6	Comparison of average strain energy release rates ( $G_{II}$ ) –specimen 1, 2 tested by using three point bending setup, specimen 3, 4, 5 by cantilever beam setup – Stitching density = 20 stitches /in <sup>2</sup> .....	78
4-7	Crack lengths corresponding to the different loads of the three-point bending setup .....	79
4-8	Moiré fringe patterns under various loading conditions of the cantilever beam setup .....	80
4-9	Relative displacements vs. positions of the three point bending setup when the load = 79.9 lbs .....	81



4-10	Relative displacements vs. positions of the three point bending setup when the load = 138.9 lbs .....	82
4-11	Relative displacements vs. positions of the three point bending setup when the load = 189.0 lbs .....	83
4-12	Comparison between two different loads of the three point beam setup .....	84
4-13	Strain energy release rate vs. crack length – stitching density = 40 stitches per square inch .....	85
4-14	Strain energy release rate vs. crack length – stitching density = 20 stitches per square inch .....	86
5-1	Mixed Mode setup – ratio of $G_I$ and $G_{II}$ is fixed .....	94
5-2	Modified mixed Mode setup – ratio of $G_I$ and $G_{II}$ is adjustable .....	95
5-3	The grip and the gripping area of a specimen .....	96
5-4	Novel setup I – by rotating a specimen to obtain different ratios of $G_I$ and $G_{II}$ .....	97
5-5	Series of pictures taken from setup I .....	98
5-6	Load vs. displacement of setup I .....	99
5-7	Novel setup II – gripping one arm of a specimen .....	100
5-8	Pictures taken from setup II .....	101
5-9	Load vs. displacement of setup II .....	102
5-10	Novel Setup III – by changing the loading position to obtain numerous ratios of $G_I$ and $G_{II}$ .....	103
5-11	Pictures taken during a test of setup III .....	104
5-12	Load vs. displacement diagrams of setup III .....	105
5-13	Relationship of $G_I^{mix}$ and $G_{II}^{mix}$ .....	106
6-1	Contours of J-integral .....	125

6-2	Loading condition of the Mode I setup .....	126
6-3	Load vs. Displacement diagram of one specimen – twenty peak loads match twenty rows of the broken stitches .....	127
6-4	Schematic of 2D solid model for stitched composites (the mesh of the actual model is much denser) .....	128
6-5	Principal strain distribution of 2D Model .....	129
6-6	Crack opening displacement (COD) vs. positions .....	130
6-7	COD vs. position close to the crack tip .....	131
6-8	Schematic drawing of the mid-plane for 2D-shell elements .....	132
6-9	Principle strain distribution in the 2D-shell model .....	133
6-10	Mises stress distribution in the 2D-shell model .....	134
6-11	Schematic drawing of the full 3D solid model for the new Mode I (the actual mesh is much denser – the thickness of the element is equal to the thickness of each layer) .....	135
6-12	Comparison of COD between the two models .....	136
6-13	Crack opening displacement (COD) vs. positions (3D model) .....	137
6-14	Strain energy density of the 2D and the 3D model around the contour .....	138
6-15	Simulation of the specimen with the twice stitch density .....	139
6-16	Novel shear test to determine the behavior of stitches under shear loading conditions .....	140
6-17	Model of stitch's behavior in Mode II .....	141
6-18	Setup for the mode II test .....	142
6-19	Schematic drawing of full 3D solid model for Mode II test (the actual mesh is much denser – the thickness of the element is equal to the thickness of each layer) .....	143
6-20	Crack opening displacement for Mode II under three different loading conditions .....	144

Abstract of Dissertation Presented to the Graduate School of the University of  
Florida in Partial Fulfillment of the Requirements for the Degree of Doctor of  
Philosophy

INVESTIGATION OF FRACTURE TOUGHNESS OF LAMINATED STITCHED  
COMPOSITES

By

Leishan Chen

August 2002

Chair: Dr. Peter G. Ifju

Cochair: Dr. Bhavani V. Sankar

Major Department: Aerospace Engineering, Mechanics and Engineering Science

The major objective of this research was to develop new test procedures to investigate the fracture toughness of laminated stitched composites. Graphite-epoxy laminated composites have very high stiffness-to-weight and strength-to-weight ratios that make them very attractive in structural applications. The properties of these materials depend strongly on fiber orientation and ratio of fiber to resin. The strength along the translaminar direction of this material is dominated by the matrix and is typically about 5% of the strength along the fiber direction. Hence, these materials are very easy to delaminate. Through-the-thickness stitching is one of the ideal ways to improve the translaminar properties and prevent crack propagation. In order to understand the stitch's effect, a series of test procedures was developed and was successfully used to test Mode I, Mode II and Mixed Mode fracture toughness of stitched laminated composites.

A secondary objective was to model stitched laminated composites to predict their properties. Finite element models were proposed to understand the effect of stitching on improving the fracture toughness for Mode I and Mode II of stitched laminated composites. From these models, "effective G" (effective strain energy release rate) and "parent G" (strain energy release rate of the parent laminate) can be isolated where stitches can be treated as "an extra structure." The "parent G" is an intrinsic parent material property and almost never changes regardless of whether the laminated composites are stitched or not. However, the "effective G" is dramatically increased by the stitching. The author also found that changing the thickness of stitches has a more profound impact on the "effective G" than changing the density of stitches.

## CHAPTER 1 BACKGROUND AND LITERATURE SURVEY

### 1.1 Background

Graphite/epoxy composite laminates have very high strength-to-weight and stiffness-to-weight ratios. They have tremendous advantages over conventional materials in applications such as aerospace and automotive structures, in which these two parameters are critical. Also, composite materials can easily be tailored to obtain desired properties in different directions and can be optimized to meet specific performance requirements. There are other advantages such as superior corrosion resistance, high energy absorption, low coefficient of thermal expansion, favorable thermal insulation and electrical resistivity. These materials have the potential to revolutionize the way present day structures are made.

However, despite the numerous potential applications, production volumes have not increased significantly in recent years. The primary deficiencies of laminated composites are their poor interlaminar strength and fracture toughness, low-impact damage resistance and impact-damage tolerance, and high processing cost. For example, the tensile strength of carbon fiber-reinforced polymer composites is between about 500 and 800 MPa in the fiber direction; but in the translaminar direction it is only 20-30 MPa since the load is predominately carried by the resin matrix. Because of the lack of translaminar reinforcement,

they generally are vulnerable to delamination which is an interface crack or a debond between two adjacent layers. Delamination can be initiated during imperfect manufacture or simply caused by the impact of a foreign body during service. Since the crack is inside the structure, it is hard to detect by visual inspection. The initial crack can grow rapidly under the subsequent application of external load. The overall stiffness and loading capability of the structure will decrease significantly. It may cause catastrophic failure of the composite structure. The poor interlaminar strength and fracture toughness of laminated composites have restricted their application in many lightweight structures.

Recently, due to adaptation of many textile technologies, the cost has been dramatically reduced. Researchers have mainly focused on how to improve the interlaminar properties of composites. Various techniques have been considered to enhance the out-of-plane properties. One of the most effective ways to increase interlaminar fracture toughness is incorporation of translaminar reinforcements. Translaminar reinforcement (TLR) has two general forms: continuous and discontinuous (Figure 1-1). Continuous weaving, knitting, braiding, rovings, threads, yarns and tows can be inserted into the lamina with the use of industrial sewing/stitching technology. Discontinuous translaminar reinforcement (in the form of short fibers, whiskers, pins, etc.) can also be used to bridge the interlaminar region. The processes of 3-D weaving, 3-D knitting and 3-D braiding generally have significant high-volume fractions of fiber in all three directions. These processes have considerably improved fracture toughness and impact properties, but these methods reduce the proportion of

fibers along the in-plane direction and create large resin pockets throughout the structure which tend to deteriorate the in-plane properties. The stitching process, on the other hand, is unique in that the stitched preform is not an integral structure because the through-the-thickness yarn is inserted into a traditional 2-D preform as a secondary process after lay-up. So, this process avoids tracking large resin pockets inside the composite. There are at least three main reasons for using stitching: i) Cost-effective method for joining fabric cloths by stitching along the preform edges which improves the ease of handling prior to liquid molding, ii) Effective method for joining composite structures to provide high in-plane and through-thickness strength and iii) Improve the interlaminar strength and toughness, and impact damage tolerance. Low-density stitching (number of stitches per square inch is less than 16) and high-density stitching (number of stitches per square inch is greater than 32) both show significant improvement of Mode I fracture toughness and moderate enhancement of Mode II fracture toughness while the in-plane properties only suffer a slight drop.

Laminated composites can be stitched as either prepreg or preform. Unfortunately, considerable fiber damage is sustained during stitching prepregs. This tends to deteriorate the properties of the composite. On the other hand, in the resin-free fabrics (preform) a needle can be easily pulled through the lamina with significantly reduced fiber damage. The type of industrial sewing machine, stitch, needle and thread are all factors that affect this stitching technique. There are two basic stitching types (Figure 1-2). One type of stitch (known as the lock stitch) is mainly used in the apparel industry. It consists of a two-thread loop

between the needle and the bobbin threads, and requires access to both the bottom and the top of the laminate. In the apparel industry, the intersection of the bobbin and needle threads is concealed in the fabric structure for aesthetic purposes. However the thread intersection in the middle of the fabric may cause a high stress concentration at the intersection point. A modified lock stitch achieved by either tensioning the bobbin thread or easing the tension in the needle thread may overcome this problem by forcing the needle thread to travel on the surface of the laminate. The modified lock stitch is more damage-tolerant since the yarn travels through the thickness of the structure. The other type of stitch is the chain stitch which has a mechanism similar to that of the lock stitch.

## 1.2 Literature Survey

Mignery et al. [1] investigated the use of stitching with Kevlar yarn to suppress delamination in graphite/epoxy laminates. Results showed that stitches effectively arrested delamination. Dexter and Funk [2] characterized the impact resistance and interlaminar fracture toughness of quasi-isotropic graphite-epoxy laminates made of unidirectional Thornel 300-6K fibers/Hercules 3501-6 resin and stitched with polyester and Kevlar yarns. They experimented with stitch parameters and found a significant drop in damaged areas of stitched laminates compared to unstitched laminates for the same impact energy. The Mode I fracture toughness, characterized by the critical strain energy release rate,  $G_{IC}$ , was found to be about 30 times higher for the stitched laminates. Ogo [3] investigated the effect of through-the-thickness stitching of plain woven graphite/epoxy laminates with Kevlar yarn. The study showed a manifold



increase in  $G_{IC}$  values at the expense of a slight drop in the in-plane properties. Pelstring and Madan [4] developed semi-empirical formulae relating damage tolerance of a composite laminate to stitching parameters. Mode I critical strain energy release rate was found to be 15 times greater than in unstitched laminates. Critical strain energy release rates decreased exponentially with increased stitch spacing. Dransfield et al. [5] investigated the effect of through-the-thickness stitching of plain woven graphite/epoxy laminates with Kevlar yarn. Their study showed a manifold increase in  $G_{IC}$  values at the expense of a slight drop in the in-plane properties. Sharma and Sankar [6] conducted a study on the effects of stitching on interlaminar fracture toughness of uniweave textile composites. They used the double cantilever beam setup to test the low density stitched specimens and the University of Florida Compression-After-Impact (UF-CAI) test fixture to investigate effects of stitching on sublaminar buckling behavior. Their study showed that stitching has a profound effect on Mode I fracture toughness and compression after impact (CAI) strength. They also found that stitching does not increase the impact load at which delaminations begin to propagate, but greatly reduces the extent of delamination growth at the end of the impact event. Jain et al. [7-9] used a double-cantilever-beam (DCB) test for stitched composites and found that the cantilever arms failed in bending before crack propagation. They used aluminum bars to bond the surfaces of the specimen to reinforce the specimen to prevent the specimen arms from failing during the DCB tests. A comparison of the specimens with tabs and without tabs showed that tabs altered the failure mechanism of the stitched thread; and that

the improvement in Mode I delamination toughness was underestimated. The fracture toughness of stitched composites had 10-fold improvement. Numerous studies [10-20] used the DCB setup to measure the Mode I fracture toughness of various stitched composites and found that the DCB setup was effective for unstitched laminates or lightly stitched composites where the stitching density is low or the stitches are not strong. However, as the stitching density increases or the strength of a stitch increases, the DCB setup doesn't work. Some researchers tried to reinforce a specimen with aluminum tabs to improve the load capability of a specimen. They faced the same problems that Jain et al. [9] encountered and found that the tabs alter the basic mechanism of a specimen and the interfaces between the tabs and the specimen are so weak that they tend to debond under high loading. After carefully studying the failure mechanism of the stitched specimens, Chen, Ifju & Sankar [21-22] found a conceptual solution for Mode I testing of heavily stitched specimens. Using this idea, the authors developed a preliminary fixture to successfully test heavily stitched specimens. Chapter 2 gives more detail about this process. Chapter 3 shows the final design of our loading fixture and some test results and analysis.

A study by Sharma and Sankar [6] showed that Mode II fracture toughness of stitched specimens increases with the delamination area bridged by stitches. They showed that in Mode II loading stitches do not break as widely expected, but deform the surrounding matrix. This deformation absorbs some energy from the system and increases the Mode II fracture toughness. Mode I and Mode II fracture studies by Sharma and Sankar [6] were concerned only with

unidirectional uniweaves where stitching was parallel to the fiber direction. Their study indicates that the interactions among stitches, fibers and matrix phase of the parent laminate are quite complicated. The mechanism has to be thoroughly understood for proper selection of stitch materials and stitch density. Jain and Mai [25] used two specimen geometries: End-Notch Flexure (ENF) geometry and End-notch cantilever geometry to analyze the effect of stitching on Mode II delamination toughness. They found that the effect of stitching on both specimen geometries is the same. Massabo and Cox [26] used the crack bridging concept to study the effect of stitching in Mode II delamination. Jain et al. [27] investigated the Mode II delamination toughness by using an end-notched flexure specimen and found that the application of the load to the unstitched specimens caused the initial delamination to grow in an unstable manner. With the addition of stitching a similar loading situation resulted in stable crack growth from the initial delamination. The improvement due to stitching was in the range of 100% to 200% with respect to unstitched specimens. It was also observed that increasing stitch thread diameter or stitch density generally led to larger improvement in Mode II toughness. Sankar and Sharma [6] used three approaches (area method, equivalent area method and classical beam theory) to calculate  $G_{IIC}$ . They determined the location of the crack tip with a microscope and an ultrasonic C-scan. Results show that an increase in apparent  $G_{IIC}$  of stitched composites was 5 to 15 times when the crack was allowed to propagate up to about the center line of the laminates. The stitches did not break during these tests. Clara and Barry [28] investigated the accuracy of the four-point

bending end-notched flexure (4ENF) test for determining Mode II delamination toughness. Results showed that the 4ENF test yields toughness similar to that obtained by ENF testing. The ENF tests performed by many researchers [29-32] showed that stitching indeed increases the delamination toughness of composites. However, because of the limitations of the ENF setup, a fully developed bridging zone is never achieved. Thus the instantaneous strain energy release rate will keep changing as the crack propagates. Chen, Ifju and Sankar [33] used a new setup (cantilever beam setup) to obtain much longer crack length. They incorporated high sensitivity moiré interferometry to determine the crack tip and the relative displacement of the two crack surfaces. Chapter 4 gives the detailed descriptions of the new setup and test results and analysis.

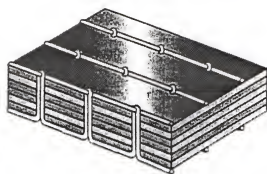
Ridards and Korjakin [34] used the traditional mixed-mode setup to test the fracture toughness of unstitched laminated composite. The ratio of Mode I and Mode II was fixed at 1.33 according to linear beam analysis. However the ratio is not constant as the crack propagates. Reeder and Crew [35-36] proposed a new mixed-mode bending method for delamination testing. In this setup, a single applied load simultaneously produces a Mode I and Mode II bending load on the specimen. This test offers numerous ratios of Mode I and Mode II and has several advantages over the traditional mixed-mode test. Shivakumar et al. [37] used a Modified Mixed Mode Flexure Specimen for the Mixed Mode I/II tests and obtained the total critical strain energy rate  $G_C$ . Then Mode I  $G_{IC}$  and Mode II  $G_{IIc}$  were separated by linear beam theory or by FE

analysis, which yields slightly higher mixed mode ratio and some dependence on crack length. Results showed some differences between the values of the critical release rates for crack initiation and aftermath. Initial  $G_c$  was lower than the average  $G$ . Chen et al. [38] modified the mixed-mode bending test apparatus and eliminated the error caused by the weight of the lever. Cox and Massabo [39] investigated the mixed mode delamination behavior of through-thickness carbon-epoxy laminates by using two different test specimens (T-stiffener and mixed-mode bending specimen). They found that small quantities of titanium or carbon z-fiber substantially improve delamination resistance in both types of specimen. Reinforcement raises the ultimate strength of the MMB specimen by a factor of three. Although many researchers [40-46] used different approaches to investigate the delamination fracture toughness of composites and to obtain useful information about the mixed mode fracture properties of composites, no researchers have successfully tested the mixed mode fracture toughness of the composites with dense translaminar reinforcement. Ifju, Chen and Sankar [47] developed three new mixed Mode setups that can be used to measure any conceivable ratio of Mode I and Mode II. Detailed setups and test results are shown in Chapter 5.

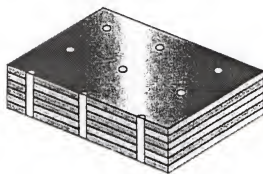
Byun et al. [48] conducted a finite element analysis of 3-D woven double cantilever beam (DCB) specimens and evaluated the Mode I critical strain energy release rate to investigate the influence of through-the-thickness fibers on crack driving force and crack length. Chen et al. [49] proposed the effective critical strain energy release rate to measure Mode I fracture toughness of stitched

laminates using a finite element model. Jain and Mai [50] have analytically modeled the Mode I and Mode II delamination toughness of stitched laminated composites. Sankar and Zhu [51] used analytical simulation to characterize the stitch's effect on laminated composites. They confirmed that stitching greatly increases Mode I fracture toughness. Sankar and Dharmapuri [52] used a simple analytical model to describe crack propagation in stitched laminated Double Cantilever Beam (DCB) specimens to obtain a closed form solution. Compared to experimental results, it is shown that inelastic behavior of the stitches plays a significant role in increasing fracture toughness due to stitching. Rhee and Lee [53] used a two-term parameter technique to calculate the energy release rate. Since this technique uses far-field stress and displacement distributions from the delamination tip, it does not require a refined mesh near the crack tip. Poursartip and Chinatambi [54] presented a method for experimental determination of the local strain energy rate based on the crack opening displacement (COD) and crack shear displacement (CSD) profiles at the crack tip for the case of Mode I and Mode II loading of composite laminates. It was found that the magnitudes of the measured COD and CSD profiles agree well with analytical linear elastic fracture mechanics (LEFM) predictions. Numerous other models [55-61] were proposed to characterize the composites' properties. These models make it convenient to change one or more parameters of composites. However, their models only give one parameter to characterize the fracture toughness of stitched composites. In Chapter 6, the author proposes two parameters to describe the fracture toughness of stitched composites – one is

$G_{\text{parent}}$  which is only related to the parent material and is constant throughout a structure. Another is  $G_{\text{eff}}$  which is not only related to the parent material but also depends on the stitches in the bridging zone. A comparison of these two parameters will show the effectiveness of stitching on the structure.



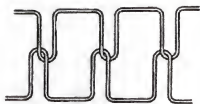
Stitching



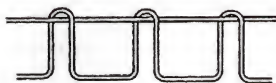
Z-pinning

Figure 1-1. Two types of translaminar reinforcement: continuous (Stitching) and discontinuous (Z-pinning).

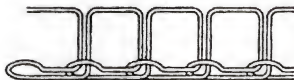




(A)



(B)



(C)

Figure 1-2. Types of Stitches: (A) lock stitch, (B) modified lock stitch, and (C) chain stitch.

## CHAPTER 2 PRELIMINARY MODE I TEST AND ANALYSIS

Through-the-thickness stitching dramatically improves the interlaminar fracture toughness of laminated composites. Currently the double cantilever beam (DCB) test is used to determine the Mode I interlaminar fracture toughness of unstitched and lightly stitched composite laminates. But the standard DCB test method is not suitable for laminates with medium to high density stitching. Because of the high bending moment at the crack tip the specimens fail due to high compressive stresses before the delamination can propagate. To overcome this limitation, a preliminary test setup, which induces axial tension in the specimen in addition to the transverse force responsible for propagation of delamination, has been developed. The axial tension reduces the compressive stresses in the vicinity of the crack tip caused by the large bending moments required for crack propagation. An analysis method has been developed to determine load-deflection and load-energy release rate relationships in the new test. The new test method has been found to be successful in testing graphite/epoxy laminates containing Kevlar stitches with a density of 64 stitches per square inch. The apparent fracture toughness of these specimens is about 45 times that of unstitched specimens.

## 2.1 Introduction

The standard DCB specimen (Figure. 2-1) is fabricated with a Teflon layer at the mid-plane to simulate an initial crack. When loaded, the crack propagates in the plane of delamination. Mode I fracture toughness can be determined using one of the two following methods. The load at which the delamination starts propagating can be used to compute the  $G_{IC}$  as

$$G_{IC} = \frac{F_c^2 a^2}{bEI}$$

where  $F_c$  is the load at which the crack propagation occurs,  $a$  is the current crack length,  $b$  is the width and  $EI$  is the equivalent flexural rigidity of the specimen. In the second method the specimen is unloaded after the crack propagates through some distance, say  $\Delta a$ . The area under the load-deflection diagram represents the work done  $\Delta W$  in propagating the crack, and the critical energy release rate is computed as

$$G_{IC} = \frac{\Delta W}{b\Delta a}$$

For instance  $G_{IC}$  of T300/3501-6 unidirectional unstitched graphite/epoxy laminates is about 1.7 lb-in/in<sup>2</sup> (298 J/m<sup>2</sup>). It should be noted when testing stitched specimens, unloading can never be complete as the broken stitches protrude out of the newly created delamination surface and prevent them from closing. In that case the author assumes that the unloading is elastic and connect the current point in the load-deflection curve to the origin.

Unfortunately, the conventional DCB test is not suitable for medium to high density stitched composites. The reason is as follows. Stitches are very

strong and large forces are required to break them or cause pullout. When the load increases, the specimen arms are subjected to large bending moments. In the end, a specimen arm fails because of micro-buckling on the compression side before crack propagation as shown in Figure. 2-2. The energy release rate in a double cantilever beam can be written as the difference in strain energy densities (strain energy per unit length of the beam) behind and ahead of the crack tip:

$$G = \frac{M^2}{bEI}$$

where  $M$  is the bending moment just behind the crack tip. Thus the bending moment required to propagate the crack varies as  $M = (G_{IC}bEI)^{1/2}$ . Because stitched laminates, even with low stitch density, exhibit about 25 times increase in fracture toughness, the bending moment required is 5 times that for unstitched laminates. This factor is even higher for medium to heavily stitched laminates. Such a high bending moment induces enormous axial stresses on the top and bottom surfaces of the sub-laminates. Because unidirectional graphite/epoxy composite has very high tensile strength, the high tensile stresses induced by the bending moment do not seem to be a problem. However failure initiates on the compressive side before the crack can propagate.

Previous researchers, for example, have suggested incorporation of reinforcing tabs as shown in Figure 2-3. Aluminum tabs bonded to the top and bottom surfaces of the specimen can increase the load carrying capability. In theory, this allows the specimen to resist larger bending moment. But, in practice, this scheme faces another problem -- when loaded, the aluminum tabs

debond from the specimen due to high interlaminar shear stresses. Further they can alter the stitch failure mechanism and the measured  $G_{IC}$  may not be the true fracture toughness.

## 2.2 Modified DCB Test

### 2.2.1 New Fixture

To avoid the aforementioned compressive failure, one must reduce the maximum compressive stresses. By adding tensile stresses along the in-plane fiber direction, the maximum compressive stresses can be suppressed. Following this idea, a preliminary fixture was developed as shown in Figure 2-4. In this fixture, heavy aluminum tabs are bonded to the specimen ends. Kevlar yarns are wound over the tabs and the specimen to prevent the specimen from pulling out of the tabs. Two rollers attached to the tabs roll over a pair of adjustable rails. As the specimen is pulled vertically, the rollers follow the path of the rails opening the specimen ligaments. Thus the transverse force that opens the crack is proportional to the tensile force applied to the specimen. The tensile force effectively cancels or reduces the compressive stresses caused by the bending moment behind the crack tip. Bearings are used in the rollers to reduce friction. Additionally, the angles of the rails are adjustable and hence the ratio between the vertical force and the horizontal force can be adjusted. For a given stitched specimen, the optimal angle can be determined. For too small angle of the rail (defined by  $\alpha$  in Figure 2-4) there is too much transverse force and the specimen breaks before the stitches break. For too large  $\alpha$  the transverse force is small and the specimen has to undergo large axial displacement before the

crack can propagate. Thus we want to find the maximum  $\alpha$  that will be able to break the stitches without breaking the specimen.

### 2.2.2 Specimen Preparation

The stitched specimens were made of 24 plies of AS4 uniweave graphite fabric and 3501-6 epoxy resin using the RTM process. Stitch yarns (bobbin yarn) were 1600 denier Kevlar (2790 yard/lb). Stitch density of the specimen was  $8 \times 1/8$  inch. We define the stitch density by the number of stitches per square inch and represent this density by the stitching pattern as (Number of stitches per inch)  $\times$  (Spacing between two stitch lines) (e.g.,  $8 \times 1/8$  inch means a stitch density of 64 where pitch is 8 stitches per inch and distance between two adjoining stitch rows is  $1/8$  inch). Needle-stitching yarn used in all the cases was Kevlar-29. Top and bottom plies of the uniweave preform were covered by one layer of plain-weave fiberglass cloth to act as the retainer cloth for the stitches. A typical test specimen was about 0.26 inch wide, 0.16 inch thick and 7 inches long. There are two rows of stitches in each specimen. The bonded areas were filed to increase the friction and the Kevlar threads were used to bond the aluminum tabs to the specimen. Screws were used to tighten the tab with the specimen and produce very high pressure between the tabs and the surfaces of the specimen to prevent slipping of the tabs from the bonded area of the specimen.

### 2.2.3 Fixture Verification

Two sets of unstitched specimens were cut from the same unidirectional 24 ply graphite/epoxy panel. Each set includes 4 specimens. One set of specimens were tested by the standard DCB method and the other by the new

fixture. Table 2.1 shows the comparison between the two methods.  $G_{IC}$  from the new method is slightly greater than that from conventional DCB tests. Because the new fixture incorporates rails and bearings, the friction in the mechanisms consumes some energy. Currently the fixture design is being modified so that friction can be kept to a minimum.

Table 2.1. Comparison of two methods

STANDARD DCB TESTS	NEW FIXTURE TESTS
Specimen1 $G_{IC}=1.63 \text{ lb}\cdot\text{in}/\text{in}^2$	Specimen1 $G_{IC}=1.78 \text{ lb}\cdot\text{in}/\text{in}^2$
Specimen2 $G_{IC}=1.81 \text{ lb}\cdot\text{in}/\text{in}^2$	Specimen2 $G_{IC}=1.97 \text{ lb}\cdot\text{in}/\text{in}^2$
Specimen3 $G_{IC}=1.57 \text{ lb}\cdot\text{in}/\text{in}^2$	Specimen3 $G_{IC}=1.99 \text{ lb}\cdot\text{in}/\text{in}^2$
Specimen4 $G_{IC}=1.67 \text{ lb}\cdot\text{in}/\text{in}^2$	Specimen4 $G_{IC}=1.77 \text{ lb}\cdot\text{in}/\text{in}^2$
<b>Average: <math>G_{IC}=1.67 \text{ lb}\cdot\text{in}/\text{in}^2</math></b>	<b>Average: <math>G_{IC}=1.88 \text{ lb}\cdot\text{in}/\text{in}^2</math></b>

#### 2.2.4 Testing of Stitched Specimens

Tests were conducted in a screw-driven universal testing machine. The crack propagation was observed by a CCD camera. A computer was used to record the images corresponding to various displacements. The load, crack extension and crack opening were determined corresponding to each displacement step. Figure 2-4 shows when the grip of the machine moves up, the bearings on the specimen follow the rails of the fixture and open up the crack surfaces. The optimum angle of the rails depends on the mechanism of particular stitched composites. The stitches typically break or pull through the composite. The horizontal components of the reactions on the bearings tend to open the crack while the vertical component provides the tensile forces to reduce

the compressive stresses induced by the bending moment. Using this fixture, we were able to test specimens with medium as well as very high stitch densities.

Typical measurements obtained using the new fixture are shown in Figure 2-6. During the test the load, displacement in the direction of applied load, crack surface opening displacement and the crack length are all measured. It should be mentioned that the crack-surface opening displacement is measured at a reference point near the end of the tabs. The crack length is defined by the distance between this reference point and the crack-tip. As a sample, the load, crack length and crack opening displacement are plotted against the axial displacement for one of the tests in Figure 2-6. From the load-displacement diagram in Figure 2-6, one can note that initially the load increases almost linearly with the displacement. When the stitches break, the crack begins to propagate and there is a sudden drop in the load. As the loading is continued, the load goes up and down as the stitches break and as the crack propagates intermittently. This saw tooth behavior of the load-deflection curve is due to the stitches breaking and new stitches offering resistance to crack propagation. The area under the load deflection curve represents the energy used in breaking the stitches and propagating the delamination.



## 2.3 Analysis

### 2.3.1 Governing Equations

The  $G_{IC}$  can be determined using one of two methods. In the first method, the area under the load-deflection diagram is divided by the crack extension area:

$$G_{IC} = \frac{\Delta W}{b \cdot \Delta a} \quad (1)$$

where  $\Delta W$  is the work of fracture,  $\Delta a$  is the crack extension and  $b$  is the width of the specimen. This method relies completely on experiments. As mentioned earlier the energy released during unloading is obtained by joining the current point in the load deflection curve to the origin.

The second method involves an elastic beam analysis of the specimen. A large deflection nonlinear analysis is performed to derive the load-deflection relationship of the test specimen. Then from the analysis results, an expression for the strain energy in the beam can be derived. The critical energy release rate at any given load (or deflection) then can be obtained as:

$$G_{IC} = -\frac{dU}{b \cdot da} \quad (2)$$

where  $U$  is the strain energy in the beam as a function of crack length  $a$ , load/deflection and other beam properties. The analysis procedure is described below.

Due to symmetry one of the ligaments of the DCB specimen (Figure 2-4) are modeled. Timoshenko beam theory, which accounts for transverse shear

deformation, is used. The two governing equations in the variables  $w$  and  $\psi$ , transverse deflection and rotation respectively, are:

$$\begin{aligned} A_{55}(\psi + \frac{\partial w}{\partial x}) &= Q \\ D \cdot \frac{\partial \psi}{\partial x} &= M + P \cdot (w_0 - w) - Q \cdot (a - x) \end{aligned} \quad (3)$$

where  $A_{55}$  is the transverse shear stiffness,  $D$  is the flexural stiffness,  $P$  is the axial load, and  $Q$  and  $M$  are the shear force and bending moment at a given cross section, and  $w_0$  is the transverse deflection at the aforementioned reference point. It may be noted that the term  $P(w_0 - w)$  accounts for the stress stiffening of the beam due to the axial force  $P$ . The solution to these equations can be derived as equation (4).

$$\begin{aligned} w &= C_1 \cdot \sinh(\lambda x) + C_2 \cdot \cosh(\lambda x) + \\ &\quad \frac{Q \cdot x}{P} + \frac{(M + P \cdot w_0 - Q \cdot a)}{P} \\ C_1 &= \frac{Q \cdot (\frac{1}{A_{55}} - \frac{1}{P})}{\lambda} \\ C_2 &= \frac{(M + P \cdot w_0 - Q \cdot a)}{P} \\ \lambda &= \sqrt{\frac{P}{D}} \end{aligned} \quad (4)$$

Once expressions for  $w(x)$  and  $\psi(x)$  are obtained the force and moment resultants can be easily derived using the beam constitutive relations. From the

results the strain energy in the beam can be calculated using numerical integration of the expression (5).

Once expressions for  $w(x)$  and  $\psi(x)$  are obtained the force and moment resultants can be easily derived using the beam constitutive relations.

From the results the strain energy in the beam can be calculated using numerical integration of the following expression:

$$U = 2 \int_0^a \left( \frac{M^2}{2EI} + \frac{P^2}{2bhE} + \frac{Q^2}{2bA_{ss}} \right) dx \quad (5)$$

Then the critical energy release rate in Equation (2) can be obtained by numerical differentiation of  $U(a)$  with respect to the crack length  $a$

### 2.3.2 Verification of the Model

Figure 2-7 illustrates the comparison of the analytical solution with the test data. The dashed line represents the crack extension vs. crack opening data from a test. We used the loads and crack extension from the test data to calculate the crack surface opening which is plotted as a solid line in Figure 2-7. The relative error between the measured opening and the calculated opening is below 10 percent. Because our analysis results are close to the experimental data, we use this method with confidence to obtain the instantaneous critical strain energy release rate  $G_{IC}$ .

### 2.3.3 Instantaneous $G_{IC}$

In this method the analysis described above is used to obtain two sets of load-deflection curves, one for a crack length  $a$  and another for  $a+\Delta a$ , where  $\Delta a$  is a small but arbitrary increment. A set of sample load-deflection curves is

shown in Figure 2-8. Then from the two curves the critical energy release rate can be obtained numerically using Equation (2). The variation of  $G_I$  as a function of the load for a given crack length is shown in Figure 2-9. The value of  $G_I$  corresponding to the load at which the crack began to propagate is the fracture toughness of the stitched specimen at that instant. This procedure can be repeated for various crack lengths and the fracture toughness can be determined as a function of the crack length. For this stitched specimen, Figure 2-10 shows the fracture toughness remains almost constant with respect to the crack length and is approximately equal to  $80 \text{ in-lb/in}^2$  ( $14,000 \text{ J/m}^2$ ). By comparing to the  $G_{IC}$  of unstitched specimens (Table 2-1), one can note that the Mode I fracture toughness increases by more than 45 times due to stitching.

## 2.4 Conclusions

A new preliminary DCB test has been developed for Mode I fracture testing of laminated composites containing a high density of through-the-thickness stitches. Conventional DCB tests are not suitable for stitched specimens, since the specimen breaks just behind the crack-tip due to high bending stresses, especially compressive stresses. In the present method a tensile stress proportional to the transverse force is induced which reduces the amount of compressive stresses. An analysis method is developed to compute the Mode I fracture toughness from the load-deflection relation. The method has been validated by testing unstitched specimens for which the fracture toughness is known, and then used to test stitched graphite/epoxy composites. The  $G_{IC}$  values for unstitched specimens were slightly greater in the present method. This

is due to frictional dissipation in the fixture. The apparent fracture toughness of specimens tested was found to be about 45 times that of unstitched specimens. Efforts are underway to modify the fixture to reduce friction and improve repeatability.

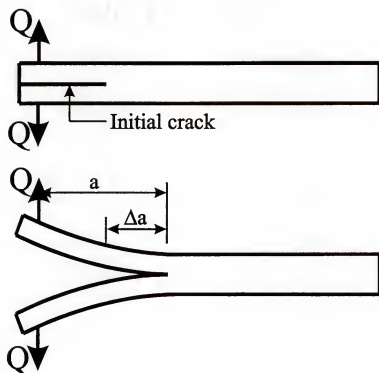


Figure 2-1. Standard DCB test method

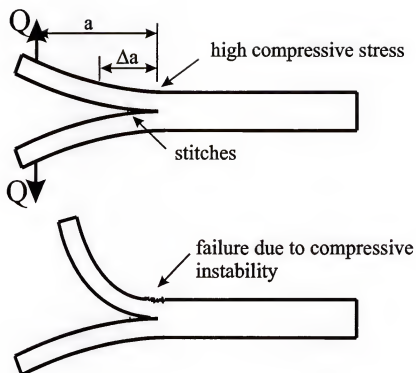


Figure 2-2. Standard DCB test for high density stitched composites

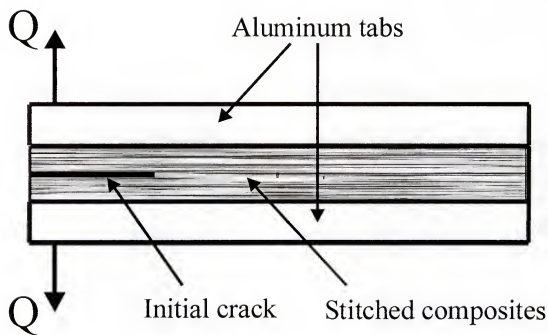
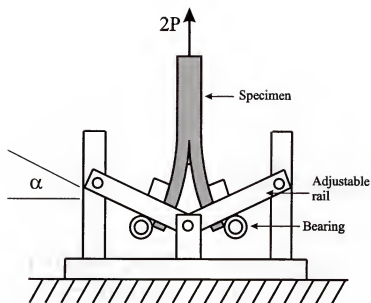
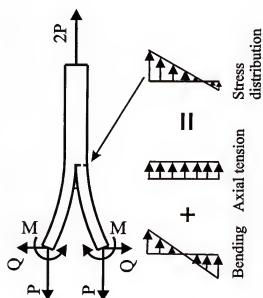


Figure 2-3. Aluminum tabs bonded over entire specimen





Modified DCB test — Fixture



Modified DCB test — Loading

Figure 2-4. Modified DCB test

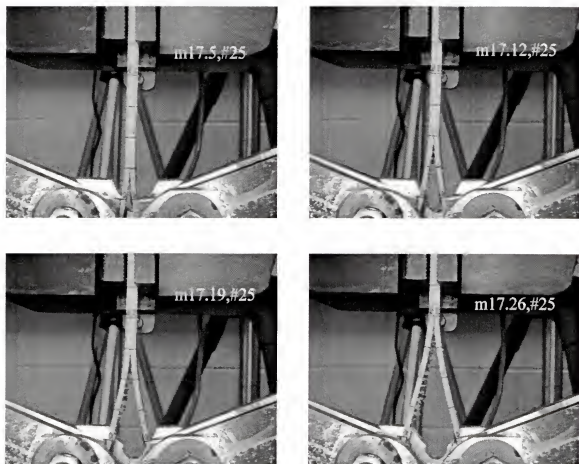


Figure 2-5. Progressive loading of the preliminary fixture

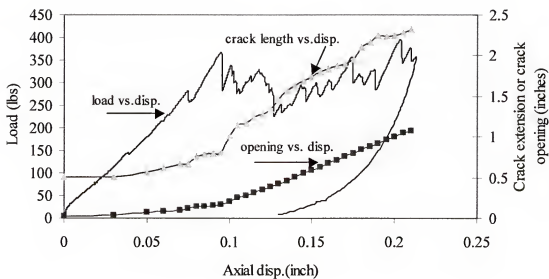


Figure 2-6. Axial displacement vs. load, crack extension and opening

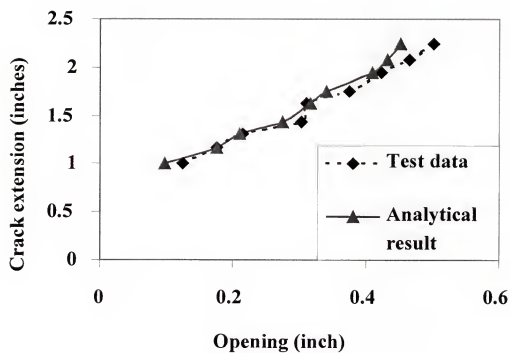


Figure 2-7. Crack extension vs. opening

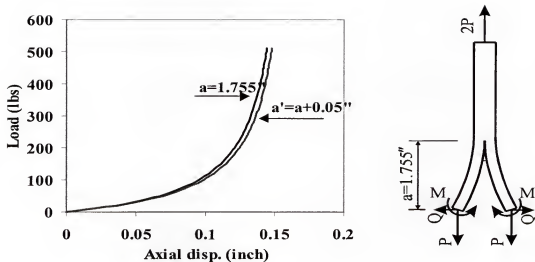


Figure. 2-8. Load vs. axial displacement under two crack lengths –  $a$  and  $a'$

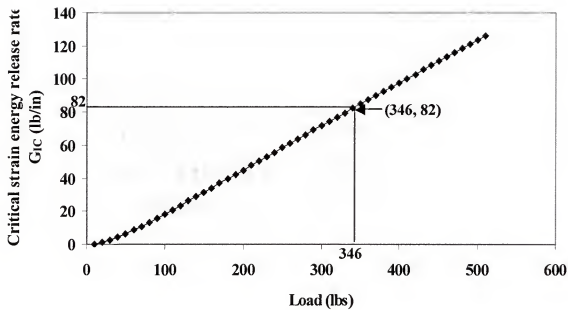


Figure 2-9. Critical strain energy release rate vs. load

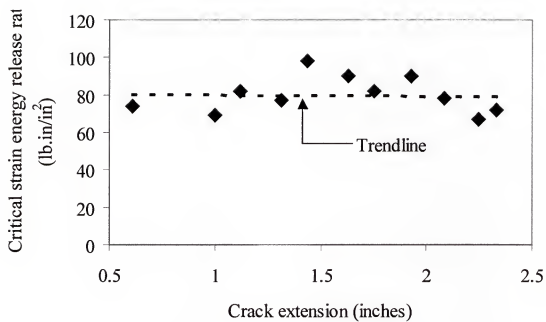


Figure.2-10. Critical strain energy release rate ( $G_{IC}$ ) vs. crack length

### CHAPTER 3

#### FINAL DESIGN OF MODE I TEST FIXTURE

Previous chapter introduced the preliminary Mode I test for stitched composites. It has been used to test the specimens with stitching density up to 64 stitches per square inch. However, this fixture has some disadvantages, for instance, the poor gripping method and the friction between the railings and bearings. After trial and error, the author developed a new fixture which overcomes the deficiencies of the prototype design. It can be very easily gripped to a specimen and can be adjustable to different thickness of specimens. Most importantly, there is no friction involved by using this new fixture. This fixture has the potential to be the standard test method for laminated composites with translaminar reinforcement. Experiments were conducted using carbon/epoxy specimens containing 6.2 stitches per square centimeter (40 stitches per square inch). The nonlinear differential equations of equilibrium of the new specimen are solved using an iterative procedure to obtain the strain energy release rate as a function of load and crack length. Results include Mode I fracture toughness, crack tip bending moment, transverse deflection and slope as a function of crack length. It is found that the apparent fracture toughness of the specimens tested remains constant as the stitches break and the crack propagates, and is about sixty times that of unstitched specimens.



### 3.1 Description of the New Test Fixture

The standard DCB specimen is depicted in Figure 2-1. The energy release rate in the DCB specimen is given by  $\frac{M^2}{bEI}$ , where  $M = Qa$  is the bending moment in one of the sub laminates at the crack tip,  $Q$  is the transverse force,  $a$  is the crack length,  $b$  is the width of the specimen and  $EI$  is the flexural rigidity of the sublaminates. As the fracture toughness of the material increases, larger bending moments are required to propagate the crack. The bending moments also produce large compressive stresses on the outer surfaces of the specimen as indicated in Figure 2-2. Although fiber composites are strong in tension, their compressive strength is limited by fiber micro-buckling, which causes the specimens to fail before the crack could propagate. One of the ways of reducing the compressive stresses is to apply a uniform tension in both arms of the DCB specimen. It should be noted that this tensile stress being equal in both arms does not contribute to the energy release rate, and Mode I crack propagation is maintained. Following this idea a new fixture has been developed as illustrated in Figure 3-1. This fixture can supply forces along two directions. The transverse component of the force is for crack opening and the axial component is for applying the tensile force. The fixture has been designed such that the initial angles of the arms are adjustable and for a given stitched specimen, the optimal angle can be determined.

A challenge in the new fixture is the design of the specimen grips that can transmit both axial and transverse forces. The conventional method of bonding the tabs to the specimen does not work as the bonded tabs cannot withstand the

large tensile and shear stresses caused by the larger load required to propagate the crack. A notch in the form of a circular arc was machined in the specimen ends as shown in Figure 3-2. The notch surface forms a 45-degree angle to the specimen surface. A pair of adjustable grips that match the notch profile in the specimen were machined out of steel (Figure 3-3.). The final assembly of the specimen and the grips is shown in Figure 3-4. Figure 3-5 shows a series of pictures taken from one of the tests. The fixture unzips the stitches one by one and the crack propagation is found to be stable.

### 3.2 Analysis of the Specimen

A schematic of the new DCB test set-up and the free-body diagram of AB are shown in Fig. 3.6. As a row of stitches breaks, the crack front reaches the location of the next row of the stitches. The current crack tip is located at Point B, and the portion of the specimen in the grip (AC in Fig. 3.6) is considered rigid. All of the forces and the bending moment at A can be expressed as:

$$\begin{aligned} F_A &= F \\ M_A &= F(L_3 \cos \theta_2 - L_4 \sin \theta_2) \sin \theta_1 - F(L_3 \sin \theta_2 + L_4 \cos \theta_2) \cos \theta_1 \\ &= FL_3 \sin(\theta_1 - \theta_2) - FL_4 \cos(\theta_1 - \theta_2) \end{aligned} \quad (1)$$

The angles  $\theta_1$  and  $\theta_2$  are indicated in Figure 3-6. The angle  $\theta_2$  is the slope at point A, i.e.,  $\theta_2 = \frac{dv(x)}{dx} \Big|_{x=L_3}$ . The angle  $\theta_1$  can be calculated using the following geometrical relations:

$$\Delta_A = \Delta_0 + L_3 * \sin \theta_2 + v_A, \quad v_A = v(x) \Big|_{x=L_3}, \quad \theta_1 = \sin^{-1} \left( \frac{L_1 - \Delta_A}{L_2} \right), \quad (2)$$

where the distance  $\Delta_0$  is indicated in Figure 3-1.

One only needs to analyze the portion  $AB$  as shown in Figure 3-6. The expression for the bending moment  $M(x)$  can be derived as

$$\begin{aligned} M(x) &= M_A + F(L_5 - x) \sin \theta_1 - F \cdot [v_A - v(x)] \cdot \cos \theta_1 \\ &= FL_3 \sin(\theta_1 - \theta_2) - FL_4 \cos(\theta_1 - \theta_2) + \\ &\quad F(L_5 - x) \sin \theta_1 - F \cdot [v_A - v(x)] \cdot \cos \theta_1 \end{aligned} \quad (3)$$

where  $v_A$  and  $v(x)$  are transverse deflections at cross section  $A$  and an arbitrary cross section at  $x$ . It must be mentioned that the calculation of bending moment  $M(x)$  in Equation (3) is exact, and the contribution of the axial force to the bending moment due to large deflection is included. The governing differential equation for the beam is:

$$\frac{1}{(1 + (dv/dx)^2)^{3/2}} \frac{d^2 v(x)}{dx^2} = \frac{1}{(1 + \theta^2)^{3/2}} \frac{d\theta}{dx} = \frac{M(x)}{EI} \quad (4)$$

where  $EI$  is the equivalent flexural rigidity of one arm of the specimen and the expression on the left hand side of the equation is exact for the beam curvature.

At this point we make the usual approximation for the curvature:

$$\frac{d^2 v(x)}{dx^2} = \frac{d\theta}{dx} = \frac{M(x)}{EI} \quad (5)$$

From the experiments (Figure 3-5) we noted that the slope of the beam is higher towards the tip of the DCB specimen where the bending moments are small. On the other hand, towards the crack tip, where the bending moment is large, the slopes are indeed small. Hence we are justified in neglecting the higher order term in the denominator for the curvature and this further simplifies the calculations.

The equivalent flexural rigidity  $EI$  was measured from a three-point bending test in which the maximum deflection  $\delta$  at the center was related to the applied force  $P$  by  $\delta = PL^3/48EI$  where  $L$  is the span of the loading fixture. The bending moment  $M(x)$  is not only a function of  $x$ , but also a function of  $\theta_1$  and  $\theta_2$ . An iterative numerical method was used to solve Equation (3). The load  $F$  and the crack length  $L_5$  are obtained from the test data. First the initial values of  $\theta_1$ ,  $\theta_2$  and  $v_A$  are calculated for the initial position of the specimen and Equation (5) was solved for  $v(x)$ . After the first iteration, new values of  $\theta_1$ ,  $\theta_2$  and  $v_A$  were calculated and used for the second round of the iteration. As the relative errors between successive sets of values of  $\theta_1$ ,  $\theta_2$  and  $v_A$  become less than an allowable minimum, say 2%, the iterations are stopped, and the final numerical values are taken as the solution. Following are steps used in the iterative process:

*Step1: import  $F$  (load),  $L_5$  (crack length) from the test.*

*Step2: use the initial values of  $\theta_1$ ,  $\theta_2$  and  $v_A$  to solve  $v(x)$ .*

*Step3: from  $v(x)$ , obtain new  $\theta_1$ ,  $\theta_2$  and  $v_A$ .*

*Step4: calculate the relative errors between new  $\theta_1$ ,  $\theta_2$  and  $v_A$  and previous  $\theta_1$ ,  $\theta_2$  and  $v_A$ . If the errors are allowable, stop and output new  $\theta_1$ ,  $\theta_2$  and  $v_A$  as the final values of  $\theta_1$ ,  $\theta_2$  and  $v_A$ . Otherwise, go to step2 by using new  $\theta_1$ ,  $\theta_2$  and  $v_A$  as input to calculate  $v(x)$ .*

From the results, the bending moment and shear force at the section just behind the crack tip can be calculated for a given load and crack length. The energy release rate is obtained from the formula:

$$G_K = \frac{1}{b} \left( \frac{M^2}{EI} \right) \quad (6)$$

where  $b$  is the width of the specimen and  $M$  is the crack tip bending moment at the instant of crack propagation. It should be noted that in order to use the aforementioned iterative method, we need to measure the crack length corresponding to the peak load in the tests.

It must be mentioned that the aforementioned approach ignores the crack bridging effects caused by the unbroken stitches in the wake of the crack tip. Such crack bridging effects in stitched composites have been considered in great detail by Massabo and Cox [26]. Sankar and Dharmapuri [52] also analytically studied the effects of bridging in stitched composite beams. In the present study there are two reasons for ignoring the bridging effects (small scale bridging). First, the size of the bridging zone is small compared to the length of the crack. Typically it was about one stitch spacing, that is, at any given time not more than two unbroken stitches were found behind the crack tip. Second, this bridging zone was found to be a constant as the crack tip moved forward. That is, there was no crack resistance effect and the fracture toughness remains constant with the crack length. Hence the present approach can be considered as a method of determining the apparent fracture toughness of the stitched composites where the micromechanics of stitch failure are not considered in detail.

### 3.3 Results and Discussion

There are two methods of determining  $G_{IC}$  from the DCB tests. In the area method the work done by the external forces on the specimen is calculated from the area enclosed by the load-deflection diagram. This work is divided by the area of crack extension to obtain the average  $G_{IC}$ . We did not use this method as the specimen could not be unloaded completely because of the protruding broken stitches on the delamination surfaces. These stitches prevented complete closure of the two ligaments of the DCB specimen. Hence it was decided to use the formula  $G_{IC} = \frac{M^2}{bEI}$  where  $M$  is the crack tip bending moment at the instant of crack propagation. The value of  $G_{IC}$  calculated using this method can also be thought of as the instantaneous fracture toughness at the time of crack propagation. However we need to know the bending moment at the crack tip from the load, crack length and other geometrical information. This is much simpler in conventional DCB specimens and can be obtained as the product of the load and the crack length. In the current specimen we need to perform an analysis to obtain the bending moment. The main difference is the effect of the axial force on the bending moment, which now is a function of the transverse deflection of the specimen. This necessitates an iterative procedure to solve for the deflection of the beam. The analysis procedure is described in the following.

The specimens were cut from a panel which is made of 4 stacks of Saertex® textile. Each stack is made of 7 layers with fiber orientations given by  $[45^\circ/-45^\circ/0^\circ/90^\circ/0^\circ/-45^\circ/45^\circ]$ . The linear density of the Kevlar stitch is 1600

denier. The specimen is 19.1 cm (7.5 inches) long and 2.0 cm (0.8 inch) wide. A sample load-deflection diagram is shown in Figure 3-7. As the stitches start breaking, one can note the fluctuations in the load and the saw-tooth like pattern of the load-deflection diagram. Each peak in the load corresponds to the breaking of one row of stitches. In the beginning the load to break the stitches increases (stitches 1 through 10), then a steady state is reached and the stitches break at a constant peak load. The twenty peak loads shown in Figure 3-7 match the twenty rows of broken stitches. After carefully observing the specimen, we found that as one row of stitches broke, the crack front reached the next row of stitches. After measuring the distance between the initial position of the crack tip and the location of  $(n+1)^{th}$  row of stitches, we can obtain the crack extension corresponding to  $n^{th}$  peak load. This peak load and the corresponding crack length ( $L_5$ ) were used as the input data in Equation (3)

The dimensions of the fixture, the specimen and the gripping area for a particular specimen (Figure 3-1 and Figure 3-6) were as follows:  $L_1=190$  mm,  $L_2=370$  mm,  $L_3=57.8$  mm,  $L_4=11$  mm,  $L_5=15.6$  mm (the crack length corresponding to the first peak load of  $P_1=3176$  N),  $b=19.05$ mm (width of the specimen),  $h=2.98$ mm (the half of the thickness of the specimen). The initial values of  $\theta_1$ ,  $\theta_2$  and  $v_A$  (the specimen in the initial position) were  $28.58^\circ$ ,  $0^\circ$  and 0, respectively. The equivalent Young's modulus of the specimen is equal to  $44.42$  GPa. After seven iterations,  $\theta_1$ ,  $\theta_2$  and  $v_A$  were equal to  $26.9^\circ$ ,  $8.8^\circ$  and 1.36 mm, respectively. The relative errors of  $\theta_1$ ,  $\theta_2$  and  $v_A$  compared to the values of sixth iteration were 1.8%, 1.7% and 1.2%, respectively.

By using the experimentally measured critical load and crack length  $AB$ , the bending moment, transverse displacement and slope along the  $AB$  can be determined by using the analytical method. For instance, we selected the tenth peak load (load=5420 N) and measured the location of the eleventh row of stitches to obtain the crack length ( $AB=44.2$  mm). Figures 3-8 through 3-10 show the bending moment, the deflection and the slope along the specimen length  $AB$ . One can note that the crack tip suffers the largest bending moment. If no axial forces were applied, the specimen would undergo micro-buckling in the vicinity of the crack-tip for this amount of the bending moment. However an axial force of 2710 N significantly reduces the compressive stresses and prevents micro buckling in the vicinity of the crack tip. The values of the bending moment can be used to calculate the critical strain energy release rate  $G_{IC}$  as shown in Equation (6).

In Figures 3-11 through 3-13 the crack-tip bending moment, shear force and  $G_{IC}$  are presented as a function of crack length for three different specimens. The average values for each specimen are shown in respective figures. The value of  $G_{IC}$  for unstitched specimen was found to be about  $300 \text{ J/m}^2$  in a previous study [1]. Thus one can note that stitching has increased the apparent fracture toughness by a factor of about 60.

### 3.4 Conclusion

A new test method has been developed for measuring the Mode I fracture toughness of laminated composites containing medium to high density stitches. The fixture is designed such that a proportional axial force is applied to the



specimen as the transverse forces on the DCB specimen increases. This prevents compressive failure of the specimen, and the crack propagates by breaking the stitches. The nonlinear differential equations of equilibrium are solved using an iterative process in order to determine the bending moment and shear force resultants for a given load and crack length. From the force resultants the critical energy release rate can be computed. The fracture toughness of the stitched graphite/epoxy specimens is found to be about 60 times that of unstitched specimens.



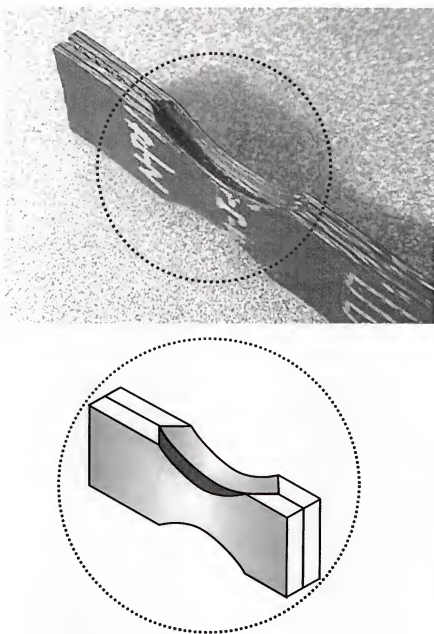


Figure 3-2. Notches in the specimen

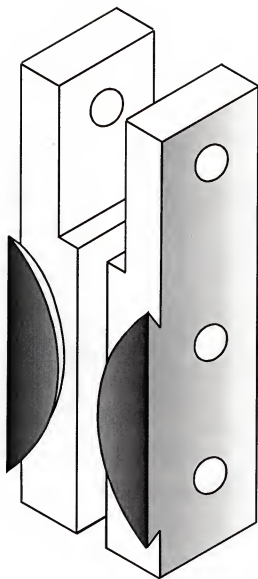


Figure 3-3. Schematic of the specimen grips. Note that the specimen grips match the notches in the specimen shown in Figure 3-2



Figure 3-4. View of the assembled specimen

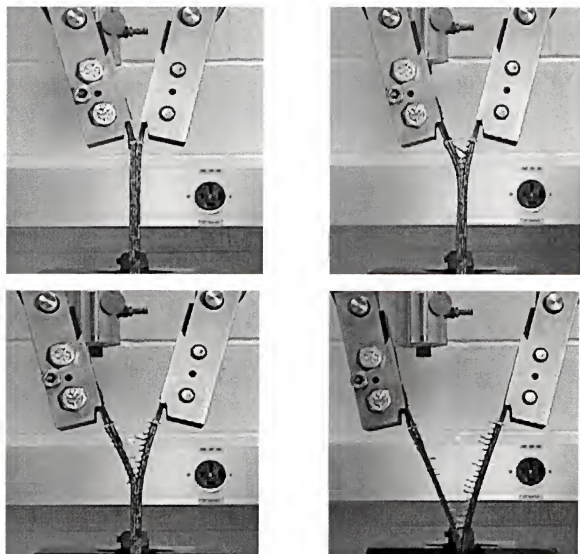


Figure 3-5. Series of pictures taken during the new DCB test

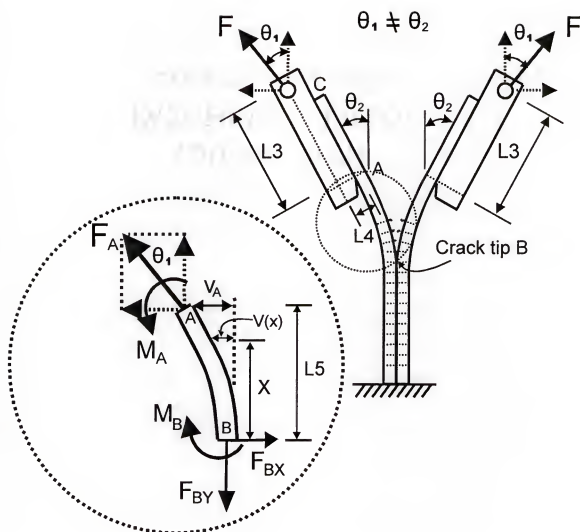


Figure 3-6. Schematic of the new DCB test setup and free body diagram of portion AB of a specimen

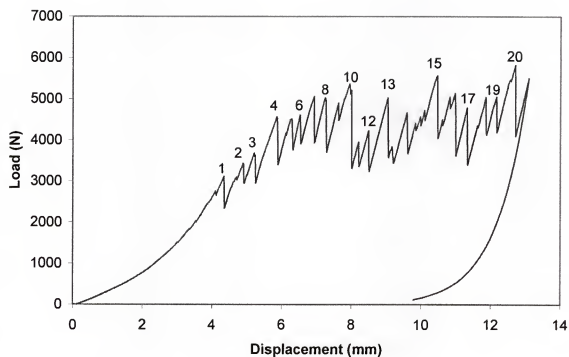


Figure 3-7. Load vs. displacement for a DCB specimen -- the twenty peak loads match twenty rows of broken stitches



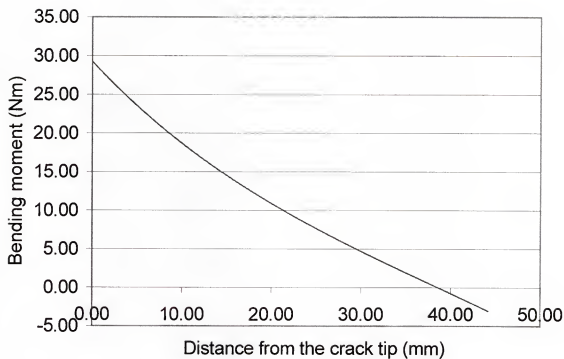


Figure 3-8. Bending moment distribution along one arm of the DCB specimen for a crack length of 44.2 mm and load of 5420 N

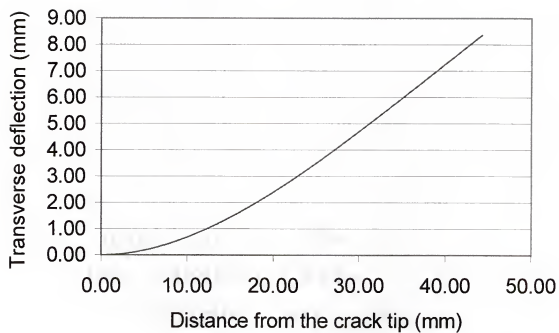


Figure 3-9. Deflection curve of one arm of the DCB specimen at a load of 5420 N and crack length of 44.2 mm

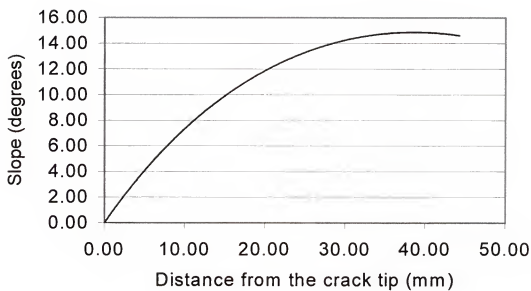


Figure 3-10. Slope vs. distance from the crack tip for crack length=44.2 mm and load=5420 N

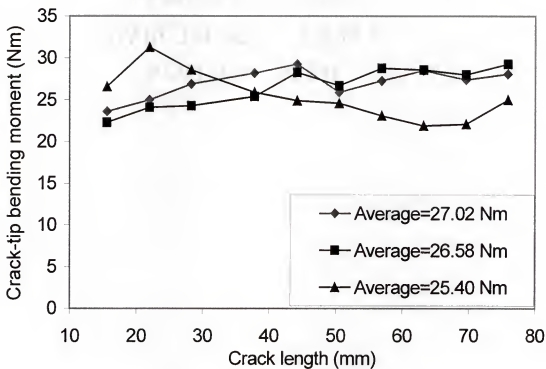


Figure 3-11. Crack-tip bending moment variation as the crack propagates. Results for three specimens are shown

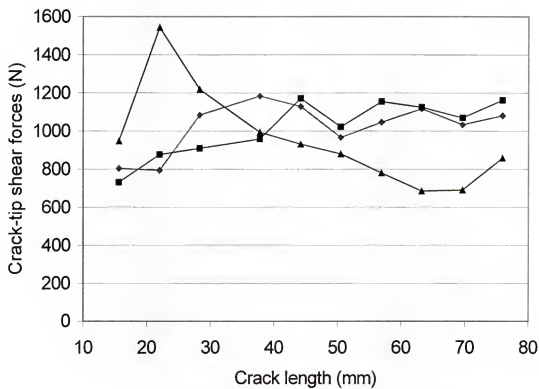


Figure 3-12. Crack-tip shear forces vs. crack length for three specimens

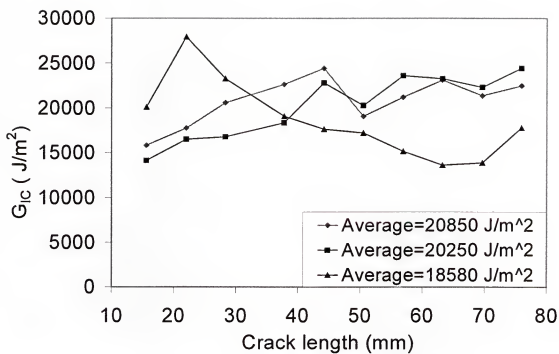


Figure 3-13. Instantaneous  $G_{IC}$  of three specimens as a function of crack length

## CHAPTER 4

### MODE II FRACTURE TOUGHNESS OF STITCHED COMPOSITES

In this chapter, two experimental approaches were used to quantify the Mode II fracture toughness of stitched composites. Currently end notched flexure (ENF) specimens are used to determine the effect of stitching on the Mode II fracture toughness of laminated composites. In ENF tests the delamination does not open, but slides. This makes it difficult to locate the crack-tip as the crack propagates and hence to estimate the length of crack propagation. This uncertainty introduces significant errors in the estimated value of the Mode II fracture toughness of stitched composite laminates. In the present study high sensitive moiré interferometry has been used to obtain the full-field displacements as well as the crack tip location in ENF specimens. By using linear elastic fracture mechanics for orthotropic material, the stress intensity factor can be determined from the relative crack surface displacements behind the crack tip. Due to high sensitivity and high resolution of this technique, the relative displacement and the crack tip can be determined precisely.

#### 4.1 Introduction

In order to fully understand the complex behavior of laminated composites with translaminar reinforcements, full-field experimental displacement analysis was performed on the microstructural scale of the materials tested in this study. To accomplish this, moiré interferometry (Post, Hahn and Ifju 1994) [24] was

used to document the mechanism of translaminar reinforcement, and their effects on damage tolerance. Moiré interferometry is a laser based optical experimental stress analysis method that is capable of revealing displacements on the sub wavelength scale. The technique of moiré interferometry is characterized by high spatial resolution, full-field information and ability to determine both normal and shear strain. By measuring the relative difference of the fringe orders between two points, the relative movement or slip between crack surfaces can be determined precisely. By plotting the displacement difference along the entire wake, the effect of stitching could be understood. Since moiré has very high spatial resolution, the location of the crack tip can be determined very accurately.

#### 4.2 End-Notched Flexure Test

Two setups, namely, three-point bending setup and cantilever beam setup are used to determine the Mode II fracture toughness of stitched composites. For the three-point bending setup, in displacement control for unstitched composites, when  $0 < a < 0.347L$ , the crack is unstable, but when  $0.347 < a < 0.5L$ , the crack is stable where  $a$  is crack length and  $L$  is total span of the three-point bending fixture. For three-point bending and cantilever beam setups, the crack is unstable for unstitched composites in load control. Hence, load control cannot be used to obtain stable crack propagation of unstitched composites in both setups. However, stability for unstitched specimens doesn't seem applicable for stitched specimen. Our tests show both setups give quite stable crack propagation for stitched composites.



#### 4.2.1 Three-Point Bending Setup

Figure 4-1 shows the standard ENF Mode II test setup. The specimens were made of AS4-3501 and fabricated with a Teflon layer at the mid-plane to simulate an initial crack. A grating, required for moiré interferometry, was replicated on the edge of the composite specimen. The specimens were cut from a panel which was made from 4 stacks of graphite/epoxy prepreg. Each stack has 7 plies which are oriented at  $[45^0/-45^0/0^0/90^0/0^0/-45^0/45^0]$ . The stitch density of the specimen was 6.2 stitches per square centimeter (40 stitches per square inch) that is the spacing between two rows of stitches was 0.51 centimeter (0.2 inch) and there were 3.15 stitches per centimeter (8 stitches per inch) in a row. The specimen was 12.7 centimeter (5 inches) long, 2.54 centimeter (1 inch) wide and 0.59 centimeter (0.230 inch) thick. The span between two supporting points was 10.2 centimeter (4 inches) and the initial crack length, or the distance from the supporting point to the crack tip, was 2.54 centimeter (1 inch).

#### 4.2.2 Cantilever Beam Setup

The disadvantage of the three-point bending setup is the limitation of the length available for crack propagation. The maximum crack length of the three point bending setup was around 2.5 cm (1 inch) therefore it was not possible to obtain a fully developed bridging zone. In order to fully understand the effect of stitches, the crack should be allowed to propagate as long as possible. The farther the crack propagates, the more the stitches become involved. In order to accomplish this, a new test setup has been developed as shown in Figure 4-2.

Using this setup, one can obtain more than 5 centimeters (2 inches) of the crack length which is equivalent up to sixteen rows of stitches. The length of a specimen for this setup was 5 centimeter (2 inch) longer than that of the Three-Point setup. Because of large deflection and rotation of the specimen, it's very difficult to apply high sensitivity moiré interferometry technique for this setup. As the sensitivity of this method is so high, small amounts of deflection and rotation will cause the fringe pattern to become too dense to photograph. After trial and error, the author found that in order to successfully run this test, a PEM-I (portable experimental moiré interferometer) should have at least three adjustments: (1) it should be able to rotate up to 13 degrees to compensate for the rotation of a specimen, (2) it should be able to move up nearly 2.5 centimeter (1 inch) to make sure the two beams cover the intended area after a specimen is deformed, (3) it should be able to move forward and backward at least 2.5 centimeter (1 inch) to trace the crack tip after crack propagation.

Figure 4-3 shows moiré interferometry fringe patterns on the edge of an ENF specimen. Both horizontal (U) and vertical (V) displacement fields are presented. By measuring the fringe order difference, the relative displacement of the two crack surfaces could be determined as a function of position along the crack.

#### 4.3 Methods of Analysis and Results

Two different methods were used to estimate the Mode II fracture toughness from the experimental results. The first one is the standard area method used in conjunction with ENF tests, and it yields the average Mode II

critical energy release rate. The second method is based on the crack surface displacements measured using high sensitivity moiré interferometry. This method yields the Mode II critical stress intensity factor. While the area method gives the average  $G_{IIC}$  over the length of crack propagation, the moiré method results in instantaneous  $K_{IIC}$  for a given crack length.

#### 4.3.1 Average Strain Energy Release Rate Using Area Method

From the moiré patterns, we can accurately document the strain distributions and relative displacements around the crack tip as well as the exact location of the crack tip which is the key to determine the crack length accurately. A simple method to obtain the average Mode II fracture toughness is to calculate the area under the load displacement diagram and then use the following equation

$$G_{II} = \frac{\Delta U}{\Delta A} \quad (1)$$

Where  $\Delta U$  is the total energy for crack propagation determined from the load-deflection diagram and  $\Delta A$  is the crack area created.

Two diagrams of the load vs. displacement of the three point bending setup are shown in Figure 4-4. One can see when the load reached about 489 N (110 pounds), the slopes of the curves started to decrease and the crack began to propagate. Due to crack propagation, the flexure modulus of the specimens gradually reduces. After the load reached about 300 pounds, the specimens were unloaded and other unloading curves were obtained. The area between loading and unloading curves represents the total energy for crack propagation.

Figure 4-5 shows the load vs. displacement diagram by using the cantilever beam setup. The displacement diagrams of these two specimens match well. When the load reached about 40 pounds, the crack started to propagate for both specimens and the slopes of the curves began to gradually decrease.

This cantilever beam setup gave us much longer final crack lengths than that of the three-point bending setup and the maximum crack lengths of the specimens vary from 1.75 to 2.75 inches. It is possible to obtain the fully developed bridging zone by using the cantilever beam setup and the maximum value of  $G_{II\text{-effect}}$  can be obtained accordingly.

Figure 4-6 gives the comparison of average strain energy release rates from the two different setups. The  $G_{II}$  of specimens 1 and 2 using the three point bending setup is little bit lower than the  $G_{II}$  of specimens 3, 4 and 5 using the cantilever beam setup. The reason is that the maximum crack lengths of specimens from the three point bending setup are much shorter than the ones from the cantilever beam setup. The more stitches that are involved, the more energy is needed to cause crack propagation. The  $G_{II\text{-ave}}$  increases about 3 to 4 times due to stitching compared to the  $G_{II\text{-ave}}$  of an unstitch specimen,

#### 4.3.2 Determining the Stress Intensity Factor by Using High Sensitivity Moire Interferometry Technique

Using the area method, one can only obtain the "average  $G_{IIC}$ ". In order to calculate the instantaneous  $G_{IIC}$ , one needs to measure the crack length as well as the load precisely. Due to stable crack propagation, the load can be read from the computer at any instant. Then we hold this load and take pictures of the

fringe patterns. From the moiré pattern, the exact location of the crack tip can be determined and hence the crack length can be measured precisely.

#### 4.3.2.1 Stress intensity factor for orthotropic brittle materials

For orthotropic materials under plane stress or plane strain conditions, the relationship between stresses and strains can be expressed as

$$\begin{aligned}\varepsilon_x &= a_{11}\sigma_x + a_{12}\sigma_y + a_{16}\tau_{xy} \\ \varepsilon_y &= a_{12}\sigma_x + a_{22}\sigma_y + a_{26}\tau_{xy} \\ \gamma_{xy} &= a_{16}\sigma_x + a_{26}\sigma_y + a_{66}\tau_{xy}\end{aligned}\quad (2)$$

The equilibrium equations for plane stress and plane strain are

$$\begin{aligned}\frac{\partial \sigma_x}{\partial x} + \frac{\partial \tau_{xy}}{\partial y} &= 0 \\ \frac{\partial \tau_{yx}}{\partial x} + \frac{\partial \sigma_y}{\partial y} &= 0\end{aligned}\quad (3)$$

The equilibrium equations will be satisfied if the stress function  $U(x,y)$  is expressed as:

$$\sigma_x = \frac{\partial^2 U}{\partial y^2}, \quad \sigma_y = \frac{\partial^2 U}{\partial x^2}, \quad \tau_{xy} = -\frac{\partial^2 U}{\partial x \partial y}\quad (4)$$

Substituting for equation (4) into the compatibility equation

$$\frac{\partial^2 \varepsilon_x}{\partial y^2} + \frac{\partial^2 \varepsilon_y}{\partial x^2} = \frac{\partial^2 \gamma_{xy}}{\partial x \partial y}\quad (5)$$

The governing differential equation of plane stress and plane strain of orthotropic materials can be obtained [29]

$$a_{22} \frac{\partial^4 U}{\partial x^4} - 2a_{26} \frac{\partial^4 U}{\partial x^3 \partial y} + (2a_{12} + a_{66}) \frac{\partial^4 U}{\partial x^2 \partial y^2} - 2a_{16} \frac{\partial^4 U}{\partial x \partial y^3} + a_{11} \frac{\partial^4 U}{\partial y^4} = 0\quad (6)$$

Defining the operators  $D_j$  ( $j = 1, 2, 3, 4$ ) as

$$D_j = \frac{\partial}{\partial y} - \mu_j \frac{\partial}{\partial x} \quad (j = 1, 2, 3, 4) \quad (7)$$

The governing equation in  $U(x, y)$  becomes

$$D_1 D_2 D_3 D_4 U(x, y) = 0 \quad (8)$$

The  $\mu_j$  are the roots of the characteristic equation

$$a_{11}\mu_j^4 - 2a_{16}\mu_j^3 + (2a_{12} + a_{66})\mu_j^2 - 2a_{26}\mu_j + a_{22} = 0 \quad (9)$$

The roots are either complex or purely imaginary and cannot be real and can be expressed as

$$\begin{aligned} s_1 &= \alpha_1 + i\beta_1, & s_2 &= \alpha_2 + i\beta_2, \\ s_3 &= \alpha_1 - i\beta_1, & s_4 &= \alpha_2 - i\beta_2 \end{aligned} \quad (10)$$

The stress function  $U(x, y)$  can be expressed in the form

$$U(x, y) = 2\text{Re}[U_1(z_1) + U_2(z_2)] \quad (11)$$

Let new functions  $\phi(z_1) = dU_1/dz_1$ ,  $\psi(z_2) = dU_2/dz_2$

The stress and displacements components can be expressed as [29]

$$\begin{aligned} \sigma_x &= 2\text{Re}[s_1^2 \phi'(z_1) + s_2^2 \psi'(z_2)] \\ \sigma_y &= 2\text{Re}[\phi'(z_1) + \psi'(z_2)] \\ \tau_{xy} &= -2\text{Re}[s_1 \phi'(z_1) + s_2 \psi'(z_2)] \\ u_x &= 2\text{Re}[(a_{11}s_1^2 + a_{12} - a_{16}s_1)\phi(z_1) + (a_{11}s_2^2 + a_{12} - a_{16}s_2)\psi(z_2)] \\ u_y &= 2\text{Re}\left[\left(\frac{a_{12}s_1^2 + a_{22} - a_{26}s_1}{s_1}\right)\phi(z_1) + \left(\frac{a_{12}s_2^2 + a_{22} - a_{26}s_2}{s_2}\right)\psi(z_2)\right] \end{aligned} \quad (12)$$

For pure Mode II,

$$\begin{aligned}
\sigma_x &= \frac{K_{II}}{\sqrt{2\pi r}} \operatorname{Re} \left[ \frac{1}{s_1 - s_2} \left( \frac{s_2^2}{\sqrt{\cos \theta + s_2 \sin \theta}} - \frac{s_1^2}{\sqrt{\cos \theta + s_1 \sin \theta}} \right) \right] \\
\sigma_y &= \frac{K_{II}}{\sqrt{2\pi r}} \operatorname{Re} \left[ \frac{1}{s_1 - s_2} \left( \frac{1}{\sqrt{\cos \theta + s_2 \sin \theta}} - \frac{1}{\sqrt{\cos \theta + s_1 \sin \theta}} \right) \right] \\
\tau_{xy} &= \frac{K_{II}}{\sqrt{2\pi r}} \operatorname{Re} \left[ \frac{1}{s_1 - s_2} \left( \frac{s_1}{\sqrt{\cos \theta + s_2 \sin \theta}} - \frac{s_2}{\sqrt{\cos \theta + s_1 \sin \theta}} \right) \right] \\
u_x &= K_{II} \sqrt{\frac{2r}{\pi}} \operatorname{Re} \left\{ \frac{1}{s_1 - s_2} [(a_{11}s_2^2 + a_{12} - a_{16}s_2)\sqrt{\cos \theta + s_2 \sin \theta} \right. \\
&\quad \left. - (a_{11}s_1^2 + a_{12} - a_{16}s_1)\sqrt{\cos \theta + s_1 \sin \theta}] \right\} \\
u_y &= K_{II} \sqrt{\frac{2r}{\pi}} \operatorname{Re} \left\{ \frac{1}{s_1 - s_2} \left[ \left( \frac{a_{12}s_2^2 + a_{22} - a_{26}s_2}{s_2} \right) \sqrt{\cos \theta + s_2 \sin \theta} \right. \right. \\
&\quad \left. \left. - \left( \frac{a_{12}s_1^2 + a_{22} - a_{26}s_1}{s_1} \right) \sqrt{\cos \theta + s_1 \sin \theta} \right] \right\}
\end{aligned} \tag{13}$$

The relationship between  $G_{II}$  and  $K_{II}$  for the orthotropic materials is:

$$G_{II} = K_{II}^2 \frac{a_{11}}{\sqrt{2}} \sqrt{\left( \frac{a_{22}}{a_{11}} \right)^{1/2} + \frac{2a_{12} + a_{66}}{2a_{11}}} \tag{14}$$

#### 4.3.2.2 Results from moiré fringe patterns of both setups

Figure 4-7 shows a series of moiré patterns under various loading conditions. The closer the distance to the crack tip, the denser the fringe pattern. These fringe patterns provide rich information. For instance, the location of the crack tip can be determined accurately and we can obtain the strain distribution around the crack tip and the relative displacement between any two points. One can see when the load is 79.9 lbs, the crack tip is behind the reference line and the crack is still in the unstitched zone. As the load reaches 138.9 lbs, the crack tip is ahead of the reference line and the crack propagates into the stitched zone.

When the load reaches 189.0 lbs, the crack tip is far ahead of the reference, the crack passes through numerous stitches.

Fringe patterns from the cantilever beam setup are shown in Figure 4-8. The stitched zone is ahead of the reference line and unstitched zone is behind the line. Similar to Figure 4-8, the crack tip is behind the reference line when the load is 31.6 lbs and crack tip is right on the line as the load reaches 31.6 lbs -- that means 31.6 lbs is the initial critical load for this specimen.

The crack surface displacements behind the crack tip of the three point bending setup are shown in Figures 4-9 – 4-11. From Figure 4-9, it may be noted that the absolute values of the upper and lower surface displacements are equal for smaller loads (79.9 lbs), but they differ significantly as the loads reach larger values (138.9 lbs and 189 lbs). This may be due to the asymmetry in the specimen about the delamination plane or the stitching effect, which needs further investigation. Since the density of fringe pattern is extremely high in the region very close to the crack tip, it's very difficult to obtain the displacement in this area. Fortunately, when one calculates the stress intensity factor, it's not necessary to select a position inside 0.5 mm (0.02 inch) of the crack zone. Similar results can be obtained from the cantilever beam setup.

#### 4.4 Stress Intensity Factor $K_{II\text{-parent}}$ and $K_{II\text{-eff}}$ and Strain Energy Release Rate $G_{II\text{-parent}}$ and $G_{II\text{-eff}}$

Usually, only the value of  $K_{II}$  or  $G_{II}$  is enough to characterize the mode II fracture toughness of a material. However, for stitched composites, as a crack propagates, stitches in the bridging zone still partially connect to the two crack surfaces. The value of  $K_{II}$  or  $G_{II}$  is not constant and is directly related to the



properties of stitches in the bridging zone. Here, author proposes two parameters, namely,  $G_{II\text{-parent}}$  and  $G_{II\text{-eff}}$  (or  $K_{II\text{-parent}}$  and  $K_{II\text{-eff}}$ ) to characterize the fracture toughness of stitched composites.  $G_{II\text{-parent}}$  is one of the intrinsic properties of the parent material and should be independent of the properties of stitches. However,  $G_{II\text{-eff}}$  is not only related to the parent material but also depends on unbroken stitches in the bridging zone. The comparison of  $G_{II\text{-parent}}$  and  $G_{II\text{-eff}}$  will show the effectiveness of stitches in laminated composites.

For the purpose of computing  $K_{II}$  using Eq. (13) we need only the relative displacements between the top and bottom crack surfaces. The relative displacements are compared for two different loads (139 and 189 lbs) in Figure 4-12. It appears that the relative displacements vary significantly with the loads. However, as one moves closer to the crack tip, say less than 1 mm (0.04 inch), the relative displacement vs. distance curves for two loads coalesce. Since we are using linear elastic fracture mechanics (LEFM) to predict the stress intensity factor  $K_{II\text{-parent}}$ , one should pick the position which is as close to the crack tip as possible. The actual locations selected to calculate  $K_{II\text{-parent}}$  are away from the process zone but still within the K-zone. Further, the coalescing of the relative displacements for those two different loads indicates that the stress intensity factor  $K_{II}$  is fairly constant for these loads which implies that the crack propagation occurs at more or less the same  $K_{II\text{-parent}}$  for the crack lengths considered. It should be mentioned that there is a relationship between  $K_{II}$  and  $G_{II}$  as shown in equation (14). We can either use  $K_{II}$  or  $G_{II}$  to represent the mode II fracture toughness of a material.

According to LEFM the strains at the crack tip should be singular, but the numerical differentiation of displacements yields finite strains at the crack tip. These values depend on the yield stress of the material, the finite curvature of the crack tip and also the location of adjacent stitches with respect to the crack tip.

Following are the material properties of the specimens used in both setups.

$$E_1 = 15.06 \times 10^6 \text{ psi}, \quad E_2 = E_3 = 1.60 \times 10^6 \text{ psi}, \quad \nu_{12} = 0.34, \quad G_{12} = 0.80 \times 10^6 \text{ psi}.$$

The layers are orientated at 45 degrees. For the plane stress the roots of the characteristic equation (9) can be obtained as

$$S_1 = 0.3033 - 0.9529i, \quad S_2 = -0.8924 - 0.4513i;$$

$$S_3 = 0.3033 + 0.9529i, \quad S_4 = -0.8924 + 0.4513i.$$

For the plan strain, the roots are

$$S_1 = 0.3541 - 0.9352i, \quad S_2 = -0.8952 - 0.4457i;$$

$$S_3 = 0.3541 + 0.9352i, \quad S_4 = -0.8952 + 0.4457i.$$

The instantaneous  $K_{IIC}$  and  $G_{IIC}$  can be calculated by equations (13) & (14). Both are assumed in the plane strain condition. Figure 4-13 shows strain energy release rate vs. crack length for laminated composite with stitching density of 40 stitches per square inch.  $G_{II}$  is a function of the positions behind the crack tip and will reach a constant value as the positions are close enough to the crack tip. This value is called  $G_{II\text{-parent}}$  and is around 3 or 4 (lb/in). When  $P=138.9$  lbs, only one row of stitches is in the bridging zone, the value of  $G_{II\text{-eff}}$  is around 10.8 lb/in as the distance behind the crack tip is more than 2.5 mm (0.1

inch). However, when  $P = 189.0$  lbs, there are more than two stitches in the bridging zone and  $G_{II-eff}$  reaches a constant value 18.0 lb/in as the distance behind the crack tip is more than 3.8 mm (0.15 inch). This indicates that the more stitches that are present in the bridging zone, the bigger the value of  $G_{II-eff}$ . As the bridging zone is "fully developed", which means the bridging zone reaches a constant value, it will only shift the location as the crack continues to propagate and  $G_{II-eff}$  reaches its maximum value. Figure 4-14 provides the strain energy release rate vs. crack length for the specimens with a stitching density of 20 stitches per square inch. The results from Figure 4-14 are from the cantilever beam setup. Using this setup, a much longer crack length can be achieved. The crack length corresponding to  $P=62.8$  lbs is about one inch and at this load, the bridging zone is more or less fully developed. One can tell from Figure 4-14 that the maximum value of  $G_{II-eff}$  is about 14 (lb/in) while the value of  $G_{II-parent}$  is about 3.5 (lb/in).  $G_{II}$  increases about 4 times for laminated composite with stitching density of 20 stitches per square inch.

A previous study by Sharma and Sankar [6] found that for unstitched graphite/epoxy laminates  $G_{IIC}$  was 600 N/m (3.42 lb/in). Thus it is clearly evident that stitching increases the fracture toughness by factors of four to six in the specimens with stitching density of 20 and 40 stitches per square inch respectively.

#### 4.5 Conclusions

Moire interferometry was used to determine the displacement field in a stitched graphite/epoxy ENF specimen. From the moire fringe patterns the

relative crack surface displacements behind the crack tip were determined. The Mode II stress intensity factor was estimated using the linear elastic fracture mechanics theory for orthotropic materials. Another estimate of fracture toughness was obtained using the area method, which provides only average value over a certain crack length. Results indicate that high sensitive moiré interferometry is very helpful in locating the crack tip during the ENF test and the relative crack surface displacement can be used to compute the instantaneous values of the Mode II fracture toughness. Stitching is found to increase  $G_{II}$ -effect by factors of four to six for stitching density of 20 and 40 stitches per square inch.

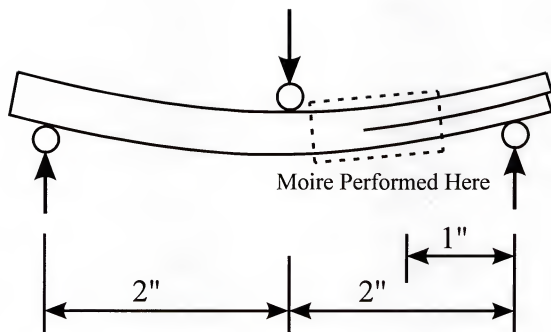


Figure 4-1. Three point bending for end notched flexure test setup

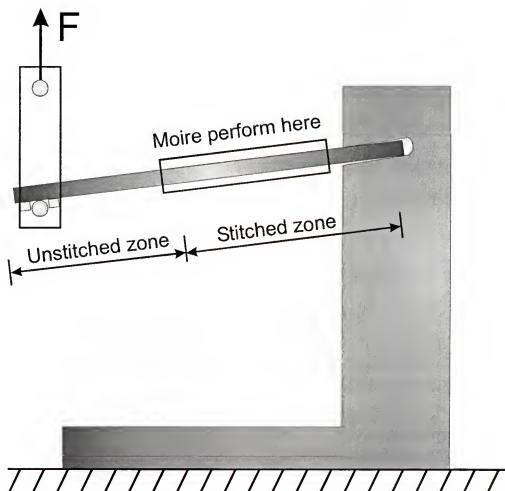


Figure 4-2. Schematic of the cantilever beam setup

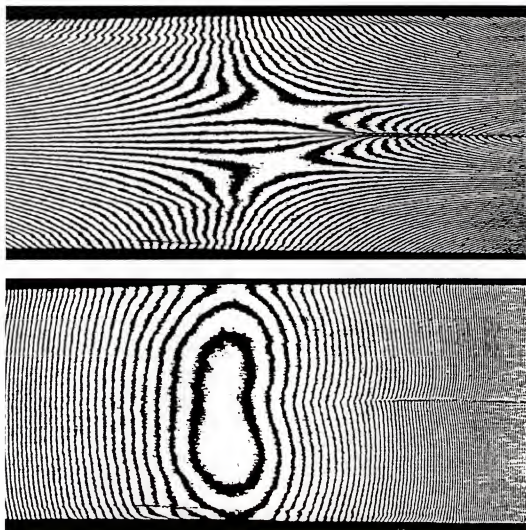


Figure 4-3. Moiré interferometry fringe patterns on the edge of an ENF specimen

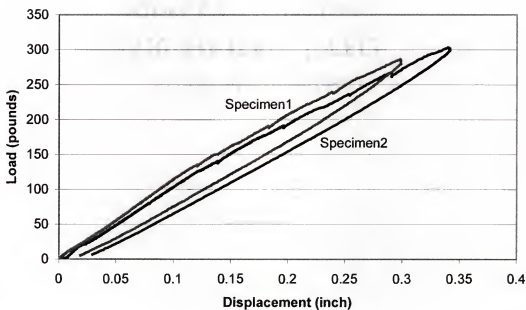


Figure 4-4. Load vs. displacement diagram of the three point bending setup



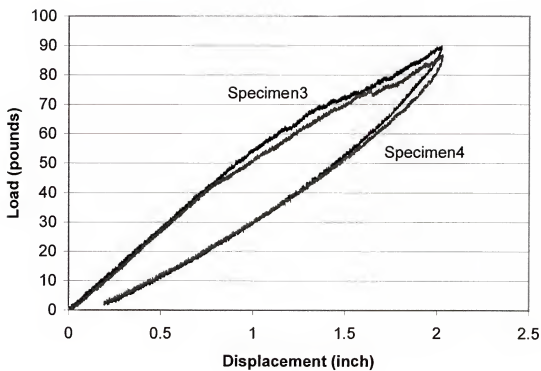


Figure 4-5. Load vs. displacement diagram of the cantilever beam setup

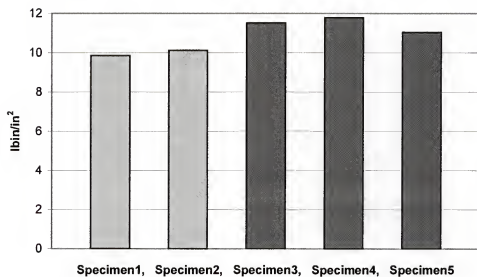


Figure 4-6. Comparison of average strain energy release rates ( $G_{II}$ ) –specimen1, 2 tested by using three point bending setup, specimen 3, 4, 5 by cantilever beam setup – Stitching density = 20 stitches /in<sup>2</sup>

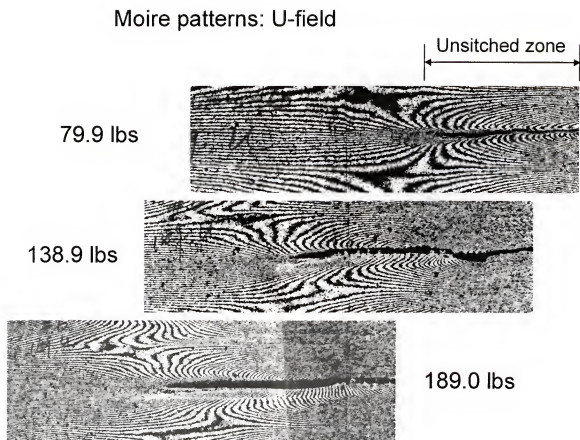


Figure 4-7. Crack lengths corresponding to the different loads of the three-point bending setup



Load = 31.6 lbs



Load = 39.7 lbs



Load = 46.7 lbs

Figure 4-8. Moiré fringe patterns under various loading conditions of the cantilever beam setup

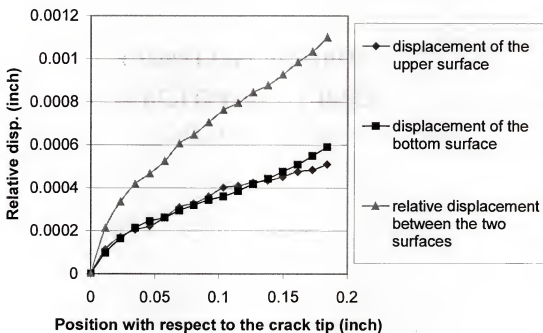


Figure 4-9. Relative displacements vs. positions of the three point bending setup when the load = 79.9 lbs

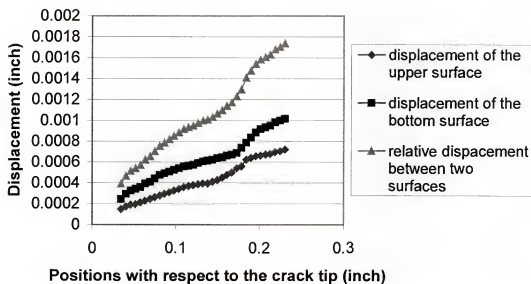


Figure 4-10. Relative displacements vs. positions of the three point bending setup when the load = 138.9 lbs

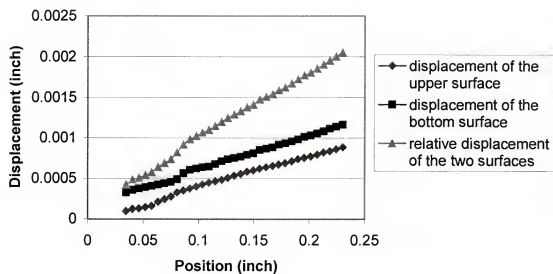


Figure 4-11. Relative displacements vs. positions of the three point bending setup when the load = 189.0 lbs

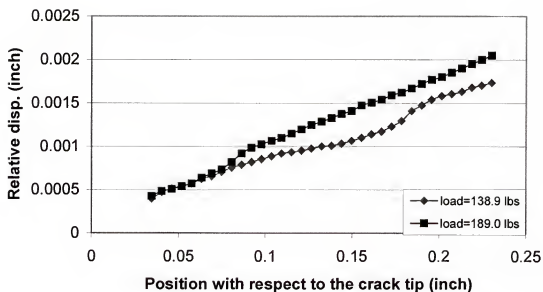


Figure 4-12. Comparison between two different loads of the three point beam setup



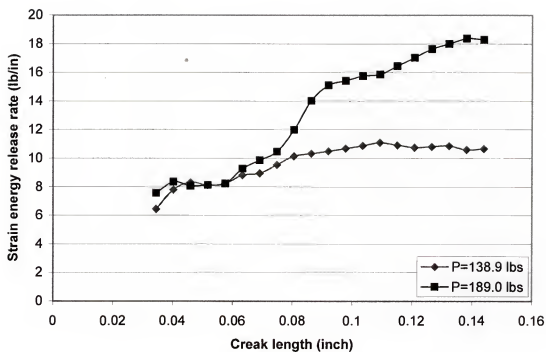


Figure 4-13. Strain energy release rate vs. crack length – stitching density = 40 stitches per square inch.

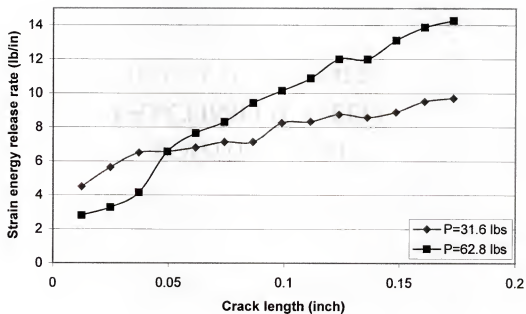


Figure 4-14. Strain energy release rate vs. crack length – stitching density = 20 stitches per square inch.

## CHAPTER 5

### NEW MIXED MODE TEST SETUPS

Until now, there has been no method to test the fracture toughness in mixed Mode loading for stitched composites. Methods that have been developed for non-stitched composites cannot be extended to test stitched composites, since stitching increases the fracture toughness beyond that which is possible to test using the existing methods. One needs to apply a high bending moment which causes the specimen to fail before crack propagation. Since mixed mode interlaminar fracture toughness is one of the most important parameters to evaluate, there is a great need to develop test methods to quantify this material property.

The author has developed three new test methods that can be used to test mixed Mode fracture toughness of stitched composites. As with the Mode I tests, the concept utilizes the idea of neutralizing the compressive stress in the specimen therefore preventing fiber buckling. The ratio of Mode I and Mode II can be adjusted to fully document the fracture toughness for any conceivable loading condition. Using this setup, one can test numerous ratios of Mode I and Mode II and plot the fracture toughness with respect to different ratios for stitched composites. These values can provide a practical way to model or design stitched composites under different loading conditions. The test method will be

introduced, load vs. displacement plots will be given and the fracture toughness of numerous ratios will be presented.

### 5.1 Introduction

The author has developed pure Mode I and pure Mode II test methods for stitched composites. However, in practical applications, it's rare to encounter pure mode I or pure mode II loading conditions since it is typical to have a combination of Mode I and Mode II loadings. Until now, no standard mixed Mode test was available for laminated stitched composites. Some researchers suggested to use the MMF specimen (Figure 5-1) [34] to test mixed Mode fracture toughness for regular laminated composites. In this setup, the ratio of Mode I and Mode is fixed at 1.33 according to linear beam analysis. Other researchers proposed the modified mixed Mode bending setup (Figure 5-2) [35-37] for different ratios of Mode I and Mode II. For this setup, numerous ratios of Mode I and Mode II can be achieved by simply moving P to different positions. These two setups are very effective for unstitched composites. Unfortunately, both methods cannot be extended to stitched composites — especially heavily stitched composites. This is due to the larger bending moment required to initiate the crack and cause crack propagation for stitched laminated composites. Typically, one arm of a specimen buckles on the compressive side under the high bending moment before the crack initiates.

### 5.2 Test Procedures

According to our analysis, a much higher bending moment is required to initiate the crack and cause crack propagation for stitched composites. In order

to avoid buckling, one needs to substantially reduce the maximum compressive stress. To maintain the high bending moment while avoiding buckling, one can apply additional tensile force to neutralize the maximum compressive stress. For Mode I testing, we developed a robust fixture which can apply both transverse and tensile forces. The transverse force is for opening the specimen and the tensile force is for reducing the maximum compressive stress. Using this fixture, we successfully tested high-density stitched composites [22-23] and measured the Mode I fracture toughness. Compared to the Mode I test, the two transverse forces in the mixed Mode test are not equal. After some iteration, we developed three new test setups which can be used to test numerous ratios of  $G_I$  and  $G_{II}$ .

### 5.2.1 Novel Setup I

The key elements of this fixture are the grips. Figure 5-3 shows the schematic drawing of the grip and the gripping area of a specimen. There is a Teflon precrack at the end of a specimen to simulate the initial crack. A picture of the assembly is shown in Figure 3-4 (Chapter 3) and the profile of the grips matches the shape of the notches of a specimen. The grips can be used for specimens ranging in thickness from 0.125 inch to 0.300 inch and the grips can hold both transverse and vertical force.

For this setup shown in Figure 5-4, if a specimen is oriented in the vertical position ( $\alpha=\beta$ ), this setup is for pure Mode I since the two transverse components ( $F_{1x}$  and  $F_{2x}$ ) are equal. But as the specimen rotates as shown in Figure 5-4, the ratio of  $F_{1x}$  and  $F_{2x}$  changes as a function of  $\alpha$  and  $\beta$ . By rotating the specimen, one can obtain numerous ratios of  $G_I$  and  $G_{II}$ . As mentioned before, the tensile

force neutralizes compression. There is a limitation for the maximum angle a specimen can rotate. If the angle is beyond this limit, one arm of the specimen will fail before crack initiation. In this case, the tensile force is not adequate to reduce the maximum compressive stress to avoid buckling. For our specimens, the maximum angle is around 15 degrees.

Figure 5-5 shows photographs of the test performed at a loading angle at  $14^{\circ}$ . Using this setup, the ratio of Mode I and Mode II can be adjusted from infinity to 7. It should be mentioned that due to the deformation of the specimen, the ratio of Mode I and Mode II will change slightly during a test. Additionally, the crack stability depends on the ratio of Mode I and Mode II and the load vs. displacement diagram (Figure 5-6) indicates the crack is unstable in this test – the total number of peak loads is less than that of the rows of stitches.

### 5.2.2 Novel Setup II

Novel setup II can be achieved by only gripping one arm of a specimen. This loading condition can be easily decoupled into the pure Mode I and pure Mode II (Figure 5-7). The ratio of Mode I and Mode II is fixed – no matter how the specimen is positioned. There are two major deficiencies of this setup - the crack is unstable and the ratio of Mode I and Mode II is fixed. Figure 5-9 shows as the load reaches the first peak load, significant energy releases and many stitches break simultaneously. If one wants to obtain the instantaneous  $G^{\max}$  (mixed Mode critical strain energy release rate), this setup is not a good choice because it's very difficult to capture the instantaneous load with respect to an exact crack length.

The ratio of Mode I and Mode II of this setup is about 1.33 and neither Mode I nor Mode II is dominant. After observing broken stitches (Figure 5-8), the author found they were roughly oriented at  $45^{\circ}$  with respect to the two crack surfaces which indicated that the combination of Mode I and Mode II caused the crack to propagate.

### 5.2.3 Novel Setup III

On the loading fixture, the bar has a series of holes (Figure 5-10) which correspond to numerous ratios of mixed Mode. At the right end of the bar a bearing reacts the horizontal force which balances the loading fixture. The free-body-diagram in Figure 5-10 shows that the ratio of Mode I and Mode II depends on the loading positions. By changing the loading positions, one can obtain different ratios of Mode I and Mode II. The ratio of Mode I and Mode II can vary from infinity to zero. The fixture can be self-balanced by adding a weight on the left side of the bar to account for errors caused by the unbalanced gravity of the fixture.

Figure 5-11 shows a series of photographs which document the fracture of a stitched specimen. Due to mixed Mode loading, the specimen bends to the left while at the same time started to open up. The effect of Mode II caused the specimen to bend to the left and the effect of Mode I opened the two arms of the specimen. The combination of Mode I and Mode II causes crack propagation. Figure 5-12 shows that the total number of rows of stitches matches the total number of peak loads and the crack propagates in a stable manner.

### 5.3 Results and Discussion

The load vs. displacement diagrams of the three setups are shown on Figures 5-6, 5-9 and 5-12. The load increases until the first row of stitches break, at which time the load drops suddenly. Subsequent rows of stitches are loaded, then break, and the cycle continues as a saw tooth. After the crack length has reached the intended value, the specimen is unloaded. The total area between the loading and unloading curves is the energy for crack propagation. One can use the area method to calculate the average strain energy release rate. For the third setup, the total number of peak loads matches the total rows of broke stitches indicating the crack is stable and one can use this setup to determine the instantaneous  $G^{mix}$ .

Table 5.1. Mixed Mode strain energy release rate of various ratio of Mode I and Mode II

Ratio ( $G_I / G_{II}$ )	<i>infinite</i>	7.15	5.33	1.33	0
$G_I^{mix}$ (lbin/in <sup>2</sup> )	42.4	44.0	34.3	19.0	0
$G_{II}^{mix}$ (lbin/in <sup>2</sup> )	0	6.2	6.4	14.2	10.7
$G^{mix}$ (lbin/in <sup>2</sup> )	42.4	50.2	40.7	33.2	10.7

Table 5-1 gives the values of  $G_I^{mix}$  and  $G_{II}^{mix}$  in different ratios of Mode I and Mode II. From Figure 5-13, one can see the values of strain energy release rate of pure Mode I and pure Mode II are not the maximum value of  $G_I^{mix}$  and  $G_{II}^{mix}$ . The maximum values of  $G_I^{mix}$  and  $G_{II}^{mix}$  occurred when the ratios were



equal to 7.15 and 1.33 respectively. From the test data, we know that the mixed Mode fracture toughness is directly related to loading conditions.

#### 5.4 Conclusion

Three novel setups were developed to measure mixed Mode properties of stitched laminated composites. These versatile setups can be used to test pure Mode I and pure Mode II as well as any ratio of mixed Mode. The fixture can be self-balanced to eliminate the error caused by the weight of the fixture. For some ratios of Mode I and Mode II, the crack is stable and hence it can be used to determine the instantaneous  $G^{\text{mix}}$  of stitched composites. Additionally, this fixture can be used to determine the mixed Mode fracture toughness for composites with translaminar reinforcement and has the potential to be a standard test method for composites with translaminar reinforcement.

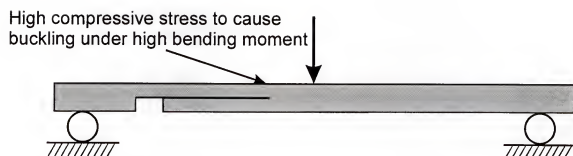


Figure 5-1. Mixed Mode setup – ratio of  $G_I$  and  $G_{II}$  is fixed.

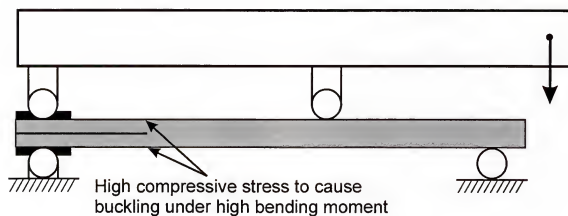


Figure 5-2. Modified mixed Mode setup – ratio of  $G_I$  and  $G_{II}$  is adjustable

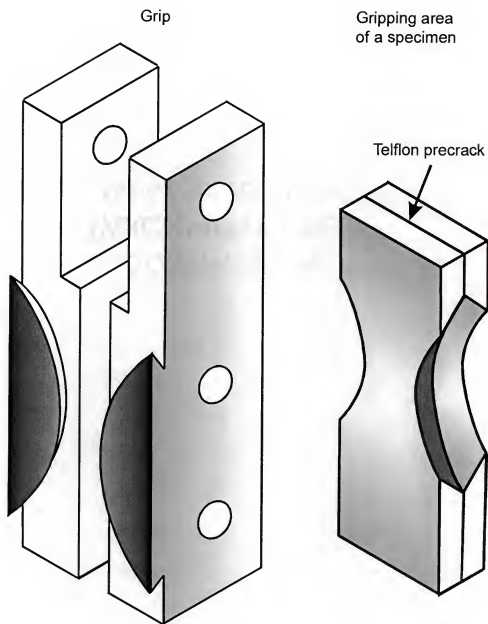


Figure 5-3. The grip and the gripping area of a specimen

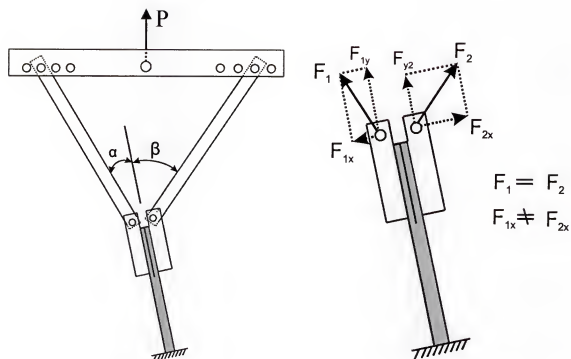


Figure 5-4. Novel Setup I – by rotating a specimen to obtain different ratios of  $G_I$  and  $G_{II}$

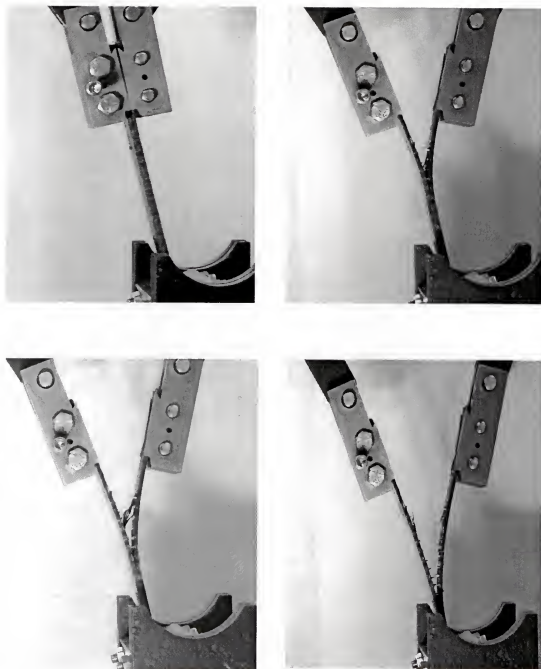


Figure 5-5. Series of pictures taken from setup I

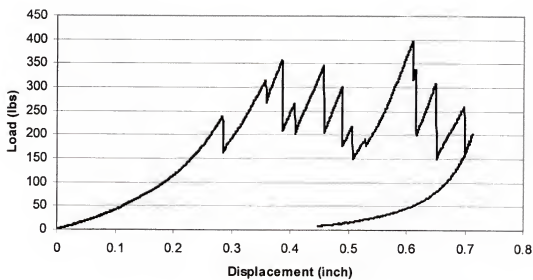


Figure 5-6. Load vs. displacement of setup I

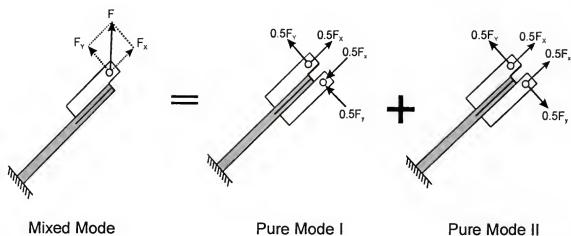


Figure 5-7. Novel setup II – gripping one arm of a specimen



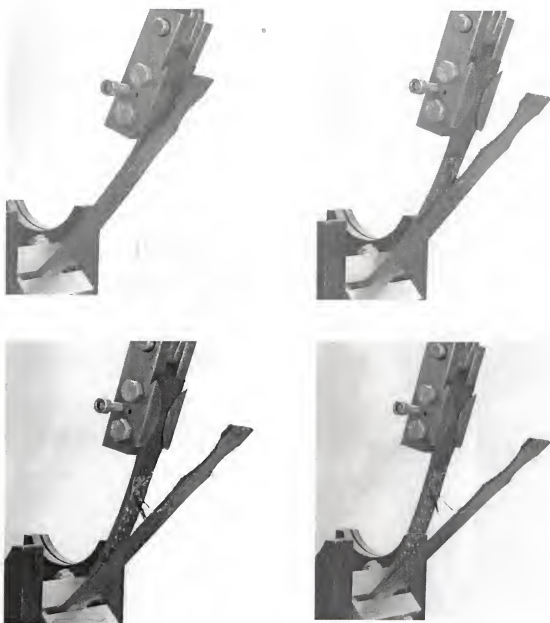


Figure 5-8. Pictures taken from setup II

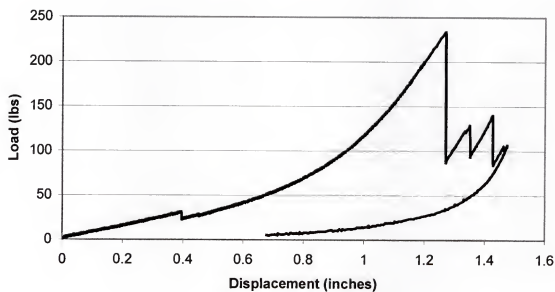


Figure 5-9. Load vs. displacement of setup II

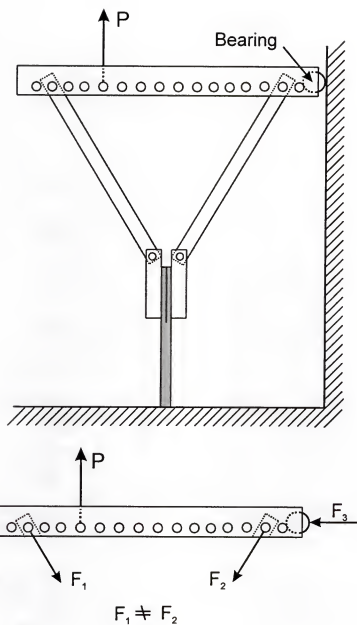


Figure 5-10. Novel Setup III – by changing the loading position to obtain numerous ratios of  $G_I$  and  $G_{II}$

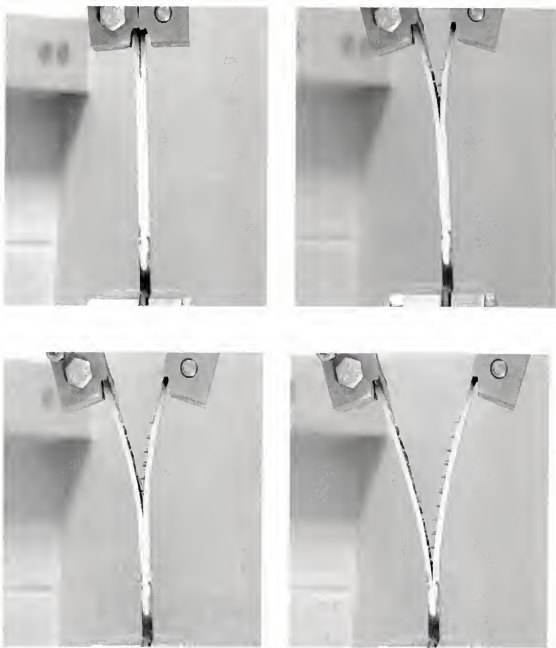


Figure 5-11. Pictures taken during a test of setup III.

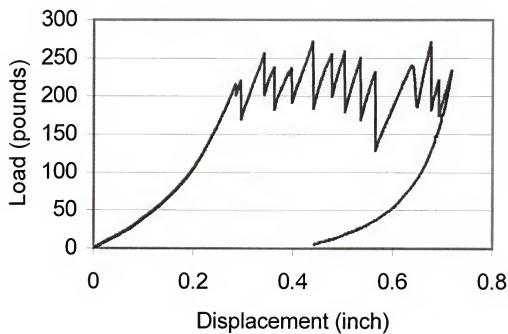


Figure 5-12. Load vs. displacement diagrams of setup III.

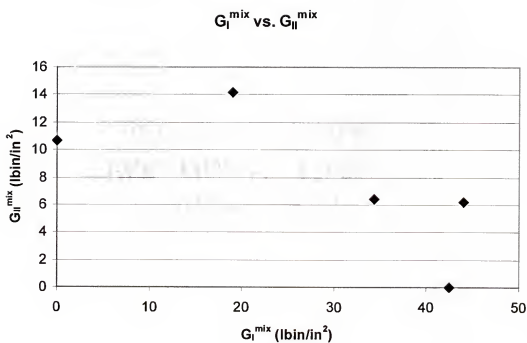


Figure 5-13. Relationship of  $G_I^{mix}$  and  $G_{II}^{mix}$ .

## CHAPTER 6

### FINITE ELEMENT ANALYSIS

The tests described in the previous sections were simulated using a finite element analysis program. The purpose of performing the finite element analysis was to identify the correct physical models that represent the stitch interactions with the parent laminate and stitch failure mechanisms. The effects of changing diameter and density of the stitch yarn can be inferred without manufacturing and testing the actual component.

The FE modeling was performed at two levels, two-dimensional models and full three-dimensional simulation. The information from experimental data was used in generating the models. Specifically, one is interested in strain energy release rate around the crack tip and stresses in the stitches in the bridging zone. The J-integral was used to calculate  $G_{\text{parent}}$  (strain energy release rate of the parent material) by using a contour which doesn't include the stitches in the bridging zone.  $G_{\text{eff}}$  (the effective energy release rate) was also calculated by the J-integral and for this purpose the contour included the stitches in the bridging zone.  $G_{\text{parent}}$  is a material property of the parent laminates and should be independent of stitch properties. However,  $G_{\text{eff}}$  not only depends on the properties of the parent laminates, but also is related to the stitches in the bridging zone. The comparison of  $G_{\text{parent}}$  and  $G_{\text{eff}}$  will give us the effectiveness of stitching in laminated composites. The results in conjunction with those from

experimental studies are expected to shed light on the micromechanics of failure initiation and propagation around the stitches

The current model assumes that the stitch interaction in DCB and ENF specimens can be modeled by linear and nonlinear bar elements. The inelastic behavior can be allowed to include the ploughing action of the stitches. In the FE 2D model, the laminates were modeled using 2D plane strain and 2D shell elements with reduced integration to reduce the hourglass effect. Results from the 2D models were compared with the full 3D models.

## 6.1 Finite Element Analysis for Mode I

### 6.1.1 Specimen

The specimen was made up of 4 stacks where each stack consisted of 7 plies which were oriented at  $[45^{\circ}/-45^{\circ}/0^{\circ}/90^{\circ}/-45^{\circ}/45^{\circ}]$ . The materials used in each stack have slightly different properties as shown in Table 6-1 and Table 6-2.

Table 6-1. One stack of materials

NUMBER OF PLIES	THICKNESS (INCH)	ORIENTATION (DEGREE)	NAME OF MATERIALS
1	0.00633	45	AS4-3501-45
2	0.00633	-45	AS4-3501-45
3	0.01285	0	AS4-3501-00
4	0.007018	90	AS4-3501-90
5	0.01285	0	AS4-3501-00
6	0.00633	-45	AS4-3501-45
7	0.00633	45	AS4-3501-45



Table 6-2. Material properties

NAME OF MATERIALS	$E_1$ (PSI)	$E_2$ (PSI)	$V_{12}$	$G_{12}$ (PSI)	$G_{13}$ (PSI)	$G_{23}$ (PSI)
AS4-3501-45	$15.04 \times 10^6$	$1.6 \times 10^6$	0.34	$0.8 \times 10^6$	$0.8 \times 10^6$	$0.52 \times 10^6$
AS4-3501-00	$15.30 \times 10^6$	$1.6 \times 10^6$	0.34	$0.8 \times 10^6$	$0.8 \times 10^6$	$0.52 \times 10^6$
AS4-3501-90	$14.88 \times 10^6$	$1.6 \times 10^6$	0.34	$0.8 \times 10^6$	$0.8 \times 10^6$	$0.52 \times 10^6$

The specimen was 7 inches long and 0.71 inch wide using stitch of 1600 denier Kevlar where there were two yarns in each stitch. The stitch density was  $8 \times 1/5$ " which means there were 40 stitches per square inch where the pitch is 1/8 inch, the spacing between two adjacent stitch rows is 1/5 inch.

#### 6.1.2 Effective Modulus $E_f$

For the parent laminates, the specimen was assumed to have both geometric and material property symmetry about the neutral surface and each ply is linearly elastic with no shear coupling. In reality, there are  $+45^\circ$  and  $-45^\circ$  plies in laminates and shear coupling should exist.

The effective modulus can be easily calculated using the laminated beam theory as

$$E_f = \frac{8}{h^3} \sum_{j=1}^{N/2} (E_x)_j (Z_j^3 - Z_{j-1}^3)$$

Here N is the total number of plies and  $Z_j$  is the distance from the neutral surface to the outside of the  $j^{\text{th}}$  ply.  $E_x$  is the modulus along the x direction and can be expressed as

$$E_x = \frac{1}{\frac{1}{E_1} \sin^4 \alpha + \left[ -\frac{2\nu_{12}}{E_1} + \frac{1}{G_{12}} \right] \sin^2 \alpha \cdot \cos^2 \alpha + \frac{1}{E_2} \sin^2 \alpha}$$

$$\alpha = 45^\circ \rightarrow E_x = 2.109 \times 10^6 (\text{psi})$$

$$\alpha = 0^\circ \rightarrow E_x = 15.3 \times 10^6 (\text{psi})$$

$$\alpha = 90^\circ \rightarrow E_x = 1.6 \times 10^6 (\text{psi})$$

Where  $E_1$ ,  $E_2$  and  $G_{12}$  are the major modulus, minor modulus and the shear modulus of each ply, respectively and  $\alpha$  is the angle between the major material axis and global x axis.  $E_x$  is very sensitive to the angle  $\alpha$  and only about 14% of  $E_x$  along  $0^\circ$  layer when  $\alpha$  is equal to  $45^\circ$ . The effective modulus ( $E_t$ ) of this specimen is equal to  $6.931 \times 10^6 (\text{psi})$  and will be used in our 2D solid model.

### 6.1.3 J-integral, "parent G" and "effective G"

J integral is defined as follows:

$$J = \int_{\Gamma} \left( U_0 n_1 - T_i \frac{\partial U_i}{\partial x_1} \right) ds$$

Here,  $U_0$  is the strain energy density,  $n_1$  is x component of the outer normal vector along the path shown in Figure 6-1 assuming crack propagation along the x direction,  $U_i$  is the displacement along the  $i$  direction and  $T_i$  is the component of the surface force along the  $i$  direction.

In Chapter 3, a new versatile fixture was used to test the stitched laminated composites. Due to the stitching, the crack propagates in a stable manner. Numerical methods were used to solve the nonlinear governing equations and the instantaneous strain energy release rates were obtained for various crack lengths. In that analysis, the nonlinear governing equation ignored

crack bridging effects caused by unbroken stitches in the wake of the crack tip. Hence that approach can be considered as a method for determining the effective fracture toughness ( $G_{eff}$ ) of stitched laminates. In order to more thoroughly understand the effect of the stitches, one should take a close look at the bridging zone where the stitches partially connect matrixes and prevent crack propagation. Three parameters ( $G_{eff}$ ,  $G_{parent}$  and COD) can be used to characterize the stitch's effect on the bridging zone.

The analytical solution has at least two drawbacks – one is that it cannot exactly model the properties of the parent materials (each layer is made of 3D orthotropic materials), second is that it cannot give the exact crack tip opening displacement (COD) around the crack tip (the behavior of COD around the crack tip is totally different from that of the position away from the crack tip).

The J-integral is typically path independent for the general case. However, due to the presence of stitches in the bridging zone, the two crack surfaces are not truly separated since they are still partially connected by the unbroken stitches. Hence, for stitched laminates, J-integral is path dependent when the bridging zone exists. If the path of contour is chosen to be very close to the crack tip, J-integral should be equal to  $G_{parent}$  which is a parent material property regardless of whether the specimen is stitched or not. On the other hand, if the path of contour includes unbroken stitches in the bridging zone, the J-integral should be equal to  $G_{eff}$  which should be larger than  $G_{parent}$  and will reach a constant value when the contour incorporates all the unbroken stitches in the bridging zone. Subsequently, as the crack continues to propagate, the

bridging zone will eventually reach a constant length and move with the crack tip. The dashed line of the contour in Fig 6.1 was used to calculate  $G_{parent}$  and the solid line of the path which includes all unbroken stitches in the bridging zone was used for calculating  $G_{eff}$ .

#### 6.1.4 2D Solid Modeling

##### 6.1.4.1 Procedure of modeling

After carefully observing Mode I specimens, the author found that all stitches were broken and no stitch was pulled out. Test results also show that there was "no ploughing" action for the Mode I test and the average breaking strength for Kevlar 1600 denier is around 78 lbs (346 N) with the failure strain of about 5 percent. There are two yarns in one stitch therefore the average failure strength of each stitch is 156 lbs (694 N). The same ultimate strength and strain can be used for all stitches and the stitch can be simply modeled as the elastic material.

The parent laminates are made of 3D orthotropic materials and the material properties are strongly dependent on the fiber orientation and there is some shear coupling effect in the laminates. In this model, instead of modeling the detailed behavior of each individual layer, "effective  $E_f$ " is used to represent the flexure modulus of the structure. It is assumed that this model can be used to accurately calculate the displacement of the laminates and the strain and stress in the stitches. However, it cannot be used to obtain the stress distribution in each ply. One should be cautious when attempting to use this model to calculate the J-integral since it is directly related to the strain energy density and

the gradient of the displacement. Later the J-integral acquired from this 2D solid model will be verified by using a full 3D simulation.

Figure 6-2 shows the loading condition of the Mode I setup where all forces transferred from the loading fixture are moved to cross section A. As the crack propagates, the crack length  $L_s$ , measured to the crack tip at B, increased accordingly. Due to stable crack propagation, the total number of peak loads matches the total number of broken rows of stitches (Figure 6-3). In this model, the author used the critical loads as well as the corresponding crack length from experiment as input data. Table 6-3 lists the 10 peak loads and the corresponding 10 crack lengths from one of the Mode I test.

Table 6-3. Input data from the experiment and analysis

	$P_1$	$P_3$	$P_5$	$P_8$	$P_{10}$	$P_{12}$	$P_{14}$	$P_{16}$	$P_{18}$	$P_{20}$
Loads (lbs)	714	835	1017	1137	1218	955	1054	1140	1076	1140
$F_x$ (lbs)	181.1	206.3	244.4	266.2	279.6	217.4	235.2	251.3	232.5	243.1
$F_y$ (lbs)	357	417.5	508.5	568.4	609.3	477.6	526.9	570.2	537.8	570.2
$M_z$ (lb-ins)	118.3	83.1	45.8	6.1	-21.7	-21.9	-49.5	-69.3	-76.6	-89.1
Crack length $h_5$ (in)	0.61	0.86	1.11	1.45	1.74	1.99	2.24	2.49	2.74	2.99

It should be mentioned that the peak loads ( $P_1 - P_{20}$ ) and the crack lengths are obtained directly from the test data. The loads ( $F_x$ ,  $F_y$ ,  $M_z$ ) at the cross section A) are calculated by an iterative method based on the geometry of the loading fixture and the properties of the specimen.

Figure 6-4 shows the schematic drawing of the 2D solid model of the new Mode I test. The mesh around the crack tip is much denser than that of other areas and in this case, more accurate COD (crack opening displacement) can be obtained around the crack tip. The stitches are connected on the top and bottom surfaces of the specimen. The position of the first row of stitches is determined under the condition – that is under one of the peak loads, the first row of the stitches is intended to reach the failure strain or stress. One can move the position of stitches back and forward in order to find the exact locations of the stitches in the bridging zone. The bending moment is applied through the equivalent couple forces  $F_M$  ( $M_Z = F_M \cdot d$ ). The corresponding location of the each peak load comes directly from the test data. In the model, there are a total 20 peak loads which correspond to 20 locations of the broken rows of the stitches.

#### 6.1.4.2 Results from 2D solid model

Figure 6-5 shows the principal strain distribution under the peak load  $P_1$  (714 lbs) and the crack length  $h_5$  (0.61 inch). There are two rows of stitches in the bridging zone. The maximum strain of the stitches in the bridging zone was 5.34% which is approximately equal to the failure strain of a stitch.

The crack opening displacement (COD) vs. position is shown in Figure 6-6. After a more detailed view in the vicinity of the crack tip, one can see that CODs are almost the same (Figure 6-6) under various loading conditions. The stress intensity factor is directly related to COD which indicates that  $G_{I\text{-parent}}$  is approximately constant under various peak loads.  $G_{I\text{-parent}}$  is an intrinsic property of the parent material and this model verifies our assumption. When the location

is close to the crack tip, COD vs. location can be roughly expressed as  $\delta_{close} = C_1 \sqrt{x}$  while moving away from the crack tip, the relationship between COD and the position is approximated as  $\delta_{away} = C_2 x^2$ . Table 6.4 gives the  $G_{I-parent}$  and  $G_{I-eff}$  by using J-integral under various loading conditions and one can see that the values of  $G_{I-parent}$  are approximately same, however  $G_{I-eff}$  varies considerably.

Table 6-4. Values of  $G_{I-parent}$  and  $G_{I-eff}$  under various loads

	P <sub>1</sub>	P <sub>3</sub>	P <sub>5</sub>	P <sub>8</sub>	P <sub>10</sub>	P <sub>12</sub>	P <sub>14</sub>	P <sub>16</sub>	P <sub>18</sub>	P <sub>20</sub>
loads (lbs)	714	835	1017	1137	1218	955	1054	1140	1076	1140
$G_{parent}$ (lb-in/in <sup>2</sup> )	2.7	3.2	4.2	5	5.6	3.6	4.2	4.7	3.3	3.6
$G_{eff}$ (lb-in/in <sup>2</sup> )	93.1	101	120.2	133	145.1	111.1	121.1	132.4	122.5	130

## 6.1.5 2D Shell Element Modeling

### 6.1.5.1 Modeling procedure

The model described in 6.1.4 uses the effective  $E_f$  to represent the global flexural modulus of the structure which provides realistic strain and displacement values. However, the model in 6.1.4 cannot be used to obtain the stress field of each layer. Due to the symmetric geometry of the specimen and small shear coupling effect, 2D shell elements are an efficient choice. The 2D shell model used here is not like the traditional plate model. From Figure 6-8, one can see that instead of using the X-Z plane, one uses the X-Y plane as the mid-plane for 2D shell elements. Hence, there are a total of 28 mid-planes with respect to 28 plies in this specimen and the "thickness of the shell element" is equal to the

"width of the specimen" (along the z direction). Since each ply is oriented in the X-Z plane, one must calculate  $E_x$  and  $E_y$  for each layer as the input properties for 2D shell elements. Table 6-5 gives the material properties for  $0^\circ$ ,  $45^\circ$  and  $90^\circ$  layers. Unlike the 2D solid model, sixth degree of freedom of the 2D shell model is active and the bending moment can be directly applied to the nodes of this model. This is not an exact model for this structure but yields useful information about the stress field in each ply.

Table 6-5. Material properties for shell elements

MATERIAL	$E_x$	$E_y$	$V_{12}$	$G_{xy}$	$G_{xz}$	$G_{yz}$
AS4-3501-00	$15.04 \times 10^6$	$1.6 \times 10^6$	0.34	$0.8 \times 10^6$	$0.8 \times 10^6$	$0.52 \times 10^6$
AS4-3501-45	$2.11 \times 10^6$	$1.6 \times 10^6$	0.34	$0.8 \times 10^6$	$0.8 \times 10^6$	$0.8 \times 10^6$
AS4-3501-90	$1.6 \times 10^6$	$1.6 \times 10^6$	0.34	$0.8 \times 10^6$	$0.52 \times 10^6$	$0.8 \times 10^6$

#### 6.1.5.2 Results and discussion

The principal strain distribution is shown in Figure 6-9. The peak load and corresponding crack length are 716 lbs and 0.61 inch respectively. Compared to Figure 6-5 of the 2D solid model under the same loading conditions, the strain field is almost identical. The maximum strains of the 2D solid model and the 2D shell model are 5.18% and 5.34% respectively. The relative difference of these two maximum strains is about 3%. If one only wants to obtain strain and displacement fields, the 2D solid model is an efficient choice. Figure 6-10 gives the Mises stress distribution in the 2D shell model. Under this loading condition, the force of the first stitch in the bridging zone is 164 lbs and this stitch is about to break or has already broken. The maximum stress on the parent laminates



happens on zero degree layers with a value 165 ksi which is less than the ultimate strength (210 ksi) of the AS4-3501 material. As the stress in the stitch reaches the failure stress under this peak load, the maximum stress of the parent laminate is still well below the failure stress.

This model indicates that our new fixture can effectively break stitches and maintain the parent laminate intact. However, this 2D shell model cannot give us the accurate J-integral around the crack tip. This is because the mid-plane used in this model is different from that of the traditional shell element. In order to obtain  $G_{I\text{-parent}}$  and  $G_{I\text{-eff}}$ , a fully three dimensional model is needed to simulate the new Mode I test.

#### 6.1.6 Three Dimensional Model

In this model, the parent laminate was modeled using 3D-orthotropic materials and stitches are modeled as bar elements. The material properties and orientation of the plies are shown in Table 6-1 and Table 6-2.

The total elements used in this 3D model are 16004. 3D solid elements are used to model the 3D orthotropic parent material and 1D bar elements are used for modeling the stitches. Because the specimen undergoes large deformation, nonlinear analysis is used to account for the nonlinear geometry during static loading. Figure 6-11 shows the schematic drawing of the fully 3D solid model of the new Mode I test. The thickness of the 3D element is equal to that of the each layer of the specimen and there are a total 28 elements through the thickness of the specimen. There is only one element through the z direction. The positions of the stitches in the bridging zone are determined by the method

used in the 2D solid model. The parallel stitches are applied on the “front surface” and the “back surface” respectively. Because the crack front is a line, the J-integral is calculated through the two lines of the nodes – one represents the nodes on the “front surface” (the nodes in front of the crack tip on the front surface) and another is the nodes on the “back surface” (the nodes in front of the crack tip on the back surface).

After the model was created, one can simply manipulate the model to move the loading positions (every peak load has an exact crack length from the test) to simulate various crack lengths. This is nearly an exact model in that one cannot exactly model the frictional forces between the stitches and the parent laminate as well as the frictional forces variation at different load stages

This 3D model can also be used to verify the 2D model discussed in the previous section. Figure 6-12 gives the comparison of COD in both models under the same peak load  $P_{12}$ . When the position is very close to the crack tip, CODs from both models are almost identical. Moving away from the crack tip, the difference increases slightly and the maximum error is still less than 8%. COD distributions under various peak loading conditions are shown in Figure 6-13 and CODs are almost the same for different peak loads when the position is close to the crack tip. The stress intensity factor is directly related to COD and this model shows that the stress intensity factors ( $K_{I\text{-parent}}$ ) are roughly the same for the various crack lengths.

Table 6-6. Comparison of  $G_{I\text{-parent}}$  and  $G_{I\text{-eff}}$  between two models

	LOAD	P1	P3	P5	P8	P10	P12	P14	P16	P18	P20
3D Model	$G_{I\text{-parent}}$ (lb-in/in <sup>2</sup> )	1.5	1.8	2.4	2.8	3.2	2.1	2.4	2.7	2.3	2.5
2D Solid Model	$G_{I\text{-parent}}$ (lb-in/in <sup>2</sup> )	2.7	3.2	4.2	5	5.6	3.6	4.2	4.7	3.3	3.6
	Relative Error	80.0%	77.8%	75.0%	78.6%	75.0%	71.4%	75.0%	74.1%	43.5%	44.0%
3D Model	$G_{I\text{-eff}}$ (lb-in/in <sup>2</sup> )	67.7	71.6	81.1	89.8	96.3	78.1	83.5	90.1	84.1	88.6
2D Solid Model	$G_{I\text{-eff}}$ (lb-in/in <sup>2</sup> )	93.1	101	120.2	133	145.1	111.1	121.1	132.4	122.5	130
	Relative Error	37.9%	41.1%	48.2%	48.1%	50.7%	42.3%	45.0%	46.9%	43.9%	45.6%

The values of  $G_{I\text{-parent}}$  and  $G_{I\text{-eff}}$  for the 2D model are not a good approximation. The relative error for  $G_{I\text{-parent}}$  and  $G_{I\text{-eff}}$  can be as high as 88% and 50%, respectively.  $G_I$  is directly related to the strain energy density and the 2D model over-predicts the strain energy. Figure 6-14 shows that  $E_x$  is only  $2.11 \times 10^6$  psi for the 3D model for  $45^\circ$  layers while  $E_f$  is  $6.11 \times 10^6$  psi for the 2D solid model. If the contour is chosen close enough to the crack tip, the strain energy of the 3D model along this contour is much lower than the strain energy of the 2D solid model under the same strain condition.

#### 6.1.7 Diameter vs. Density of Stitches

The stitch cross-sectional area and the density are the two most important factors when stitches are chosen as reinforcement. Which parameter, diameter or density, has more profound influence on the  $G_{I\text{-eff}}$ ? We use our 2D solid model to vary these two parameters and answer this question.

First, the density of stitching is doubled and the denier of Kevlar is maintained. In order to obtain the effective energy release rate ( $G_{I-eff}$ ),  $G_{I-parent}$  should be fixed. We change the loading conditions and the distance between the first stitch and the crack tip shown in Figure 6-15 until the stress of the first stitch in the bridging zone reaches the ultimate stress and  $G_{I-parent}$  is equal to the value obtained from the original specimen. After the new  $L_{s2}$  and the new critical loading condition are determined,  $G_{I-eff}$  is calculated.

Second, the cross-sectional area of a stitch is doubled and the density of stitching is maintained. Following the same procedure described in the previous section, as the new  $L_{s2}$  and the new critical load are determined,  $G_{I-eff}$  can be calculated accordingly.

Table 6-7 provides results for these two simulations and it is apparent that increasing the cross-sectional area of the stitch has a more profound influence on  $G_{I-eff}$ .  $G_{I-eff}$  increases 56.4% as the cross section is doubled while  $G_{I-eff}$  only increases 28.1% with twice the stitch density.

Table 6.7.  $G_{I-eff}$  under two simulations

Original specimen with 1600 denier Kevlar and the stitching density 8x1/5	123.5 (lbin/in <sup>2</sup> )	
Simulation of the specimen with the twice stitch density	158.2 (lbin/in <sup>2</sup> )	Relative increase 28.1%
Simulation of the specimen with the doubled cross-sectional area of stitches	193.2 (lbin/in <sup>2</sup> )	Relative increase 56.4%

## 6.2 Finite Element Model for Mode II

### 6.2.1 Modeling Procedure

Experiments revealed that for Mode II tests, there is a ploughing action between the stitches and the matrix. Additionally, the stitches seem to undergo elastic to perfect plastic behavior before breaking. These observations were made during tests with a novel shear test shown in Figure 6-16.

An extensometer was mounted on this novel shear loading fixture (Figure 6-16) to document the relative displacement between the crack surfaces. When the relative displacement reached 0.0032 inch (0.08 mm), the load on a stitch reached the maximum value 67.25 lbs. The failure relative displacement of a stitch is about 0.008 inch (0.2 mm).

The behavior of a stitch in Mode II loading is total different from that in Mode I loading. In the Mode I test, there is no ploughing action between stitches and the parent laminate, however in Mode II, the stitches plough through the matrix which creates local damage of the parent laminate. Although the stitch itself does not undergo plastic deformation, the ploughing action can still be simulated as the plastic deformation of a stitch (Figure 6-17).

The specimen used for the Mode II test was 6.5 inches long and 1 inch wide. Figure 6-18 shows the Mode II test setup and the initial crack length of the specimen was 2.95 inches. After loading, the two crack surfaces contact each other and the coefficient of friction between them was assumed to be 0.15. High sensitivity moiré interferometry [24] was used to determine the crack lengths and the relative displacement between the two crack surfaces. Table 6-8 lists 6 peak

loads with respect to 6 crack lengths.  $G_{II\text{-parent}}$  can be determined by J-integral with a contour which is in the wake of the vicinity of the crack and doesn't include the unbroken stitches in the bridging zone while  $G_{II\text{-eff}}$  can be calculated by a contour which includes all the unbroken stitches in the bridging zone. As the crack propagates, both  $G_{II\text{-parent}}$  and  $G_{II\text{-eff}}$  can be obtained under various peak loads using the J-integral.

Table 6-8. Loads and crack lengths of Mode II test.

	P1	P2	P3	P4	P5	P6
Load (lbs)	31.6	39.7	46.7	52.4	62.6	62.8
Crack length (inch)	2.95	3.03	3.1	3.2	3.54	3.87

Figure 6-19 shows the schematic drawing of the full 3D solid model of the new Mode II test. Like the 3D model for Mode I test, the thickness of the 3D element is equal to that of the each layer of the specimen and there is only one element through the z direction. The mechanism of the stitches in the Mode II test is totally different from that of the Mode I test. Due to the ploughing effect between the stitches and matrix, one cannot directly connect a stitch to the top and the bottom surfaces of a specimen (in this case, it cannot reflect the behavior of the stitches in Mode II test). Instead, "very short bar elements" oriented along the crack surfaces are used to simulate the interaction between the stitches and the matrix. The length of the bar element is 0.05 inch (0.125 mm). From the new loading fixture (Figure 6-16), the stitches' behavior in the Mode II test can be idealized as an elastic and perfect material shown in Figure 6-17. It should be

emphasized that the number of the stitches in the bridging zone depends on the crack length and the loading conditions. For instance, under the peak load  $P_5$  there are 3 rows of the stitches in the bridging zone while under the peak load  $P_6$  there are 4 rows of the stitches in the bridging zone. This model can also be used to simulate the numerous conditions, for instance, increasing the density of the stitches, increasing the thickness of the stitches or even changing the material properties and the orientations of the each layer. The previous full 3D model for the new Mode I test was used to simulate two conditions – doubling the density of the stitching and doubling the cross section of a stitch. One can repeat the same process for this Model.

### 6.2.2 Results and Discussion

Figure 6-20 shows CODs under three peak loads when the position is very close to the crack tip. They are almost the same. These results, again, verify our assumption – that  $G_{II\text{-parent}}$  is a parent material property and should be constant throughout a structure. Two parameters,  $G_{II\text{-parent}}$  and  $G_{II\text{-eff}}$  can be used to characterize the strain energy release rate of stitched laminates.

Table 6.9. Comparison of  $G_{II\text{-parent}}$  and  $G_{II\text{-eff}}$  under different loading conditions

LOAD	P1	P2	P3	P4	P5	P6
$G_{II\text{-parent}}$ (lb-in/in <sup>2</sup> )	1.4	1.5	1.6	1.9	1.6	1.2
$G_{II\text{-eff}}$ (lb-in/in <sup>2</sup> )	1.7	2.6	3.7	4.6	5	3.9

Table 6-9 makes the comparison of  $G_{II\text{-parent}}$  and  $G_{II\text{-eff}}$  under different loading conditions. The Effective Mode II fracture toughness is strongly

dependent on the crack length and the number of stitches in the bridging zone. Usually, the more stitches that are involved in the bridging zone, the larger the  $G_{II-eff}$ . We expect that as the crack continues to grow, the first row of stitches will finally break and at this moment the bridging zone will reach its maximum length. After that,  $G_{II-eff}$  will reach the maximum value and will remain approximately constant as the crack continues to propagate.



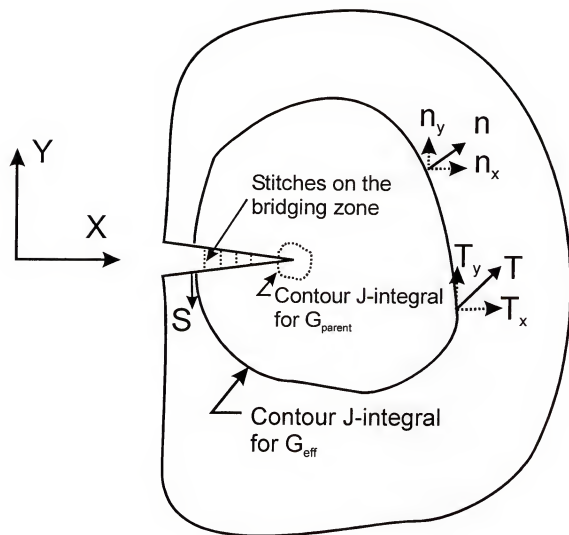


Figure 6-1. Contours of J-integral

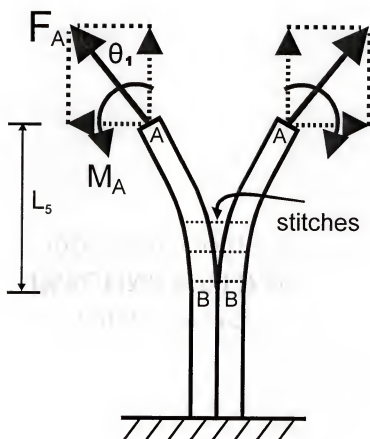


Figure 6-2. Loading condition of the Mode I setup.

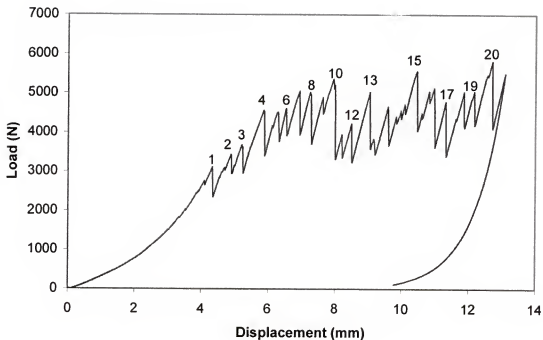


Figure 6-3. Load vs. Displacement diagram of one specimen – twenty peak loads match twenty rows of the broken stitches

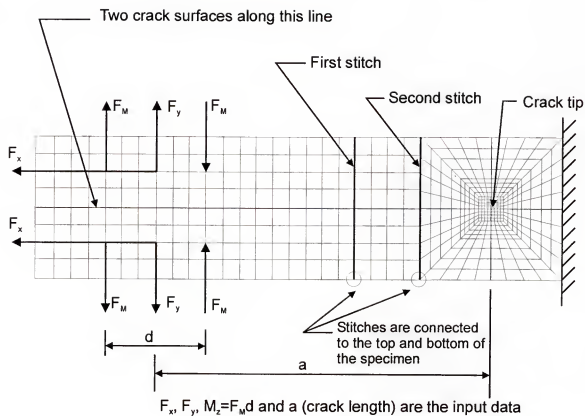


Figure 6-4. Schematic of 2D solid model for stitched composites (the mesh of the actual model is much denser)

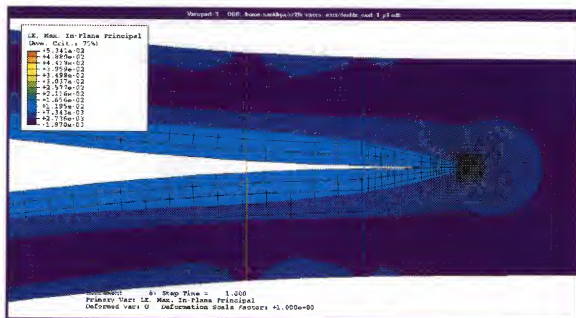


Figure 6-5. Principal strain distribution of 2D Model.

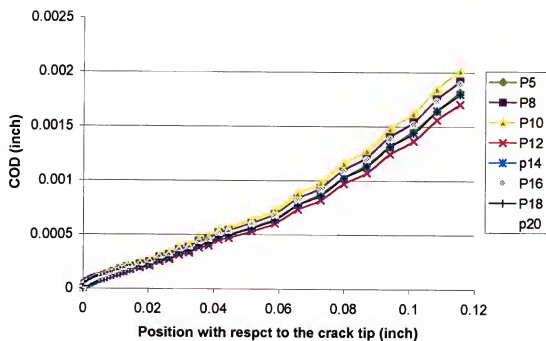


Figure 6-6. Crack opening displacement (COD) vs. positions

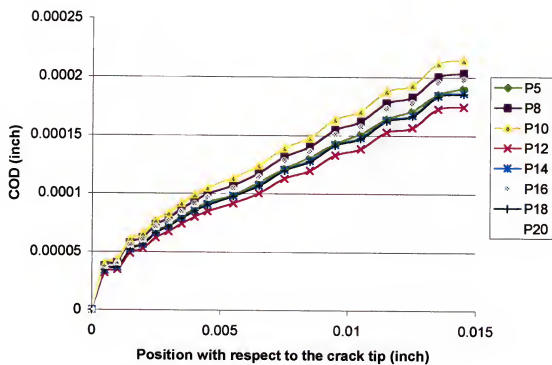


Figure 6-7. COD vs. position close to the crack tip

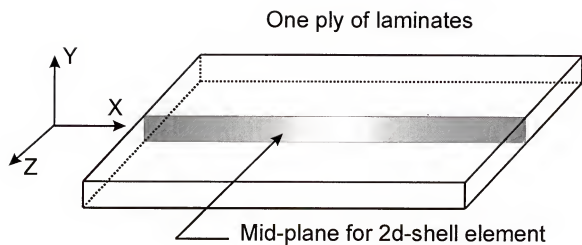


Figure 6-8. Schematic drawing of the mid-plane for 2D-shell elements





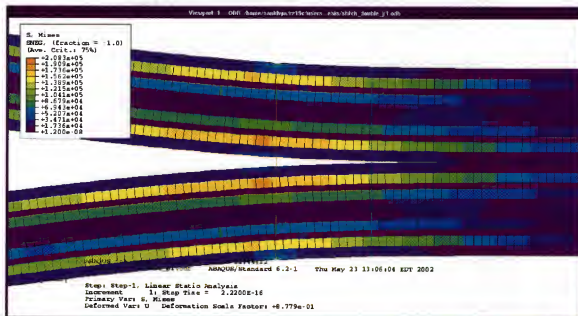


Figure 6-10. Mises stress distribution in the 2D-shell model

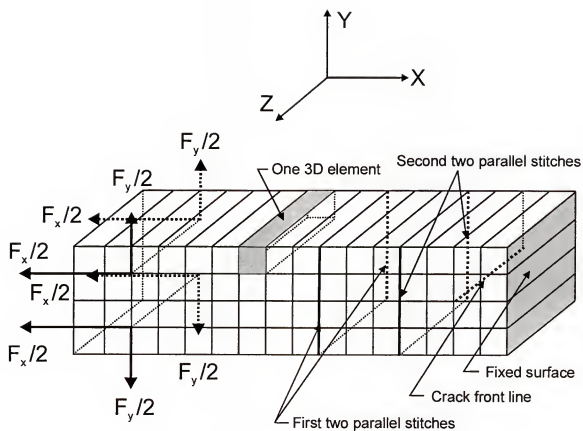


Figure 6-11. Schematic drawing of the full 3D solid model for the new Mode I (the actual mesh is much denser – the thickness of the element is equal to the thickness of each layer)

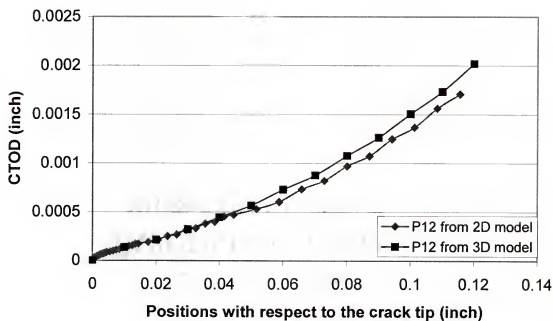


Figure 6-12. Comparison of COD between the two models

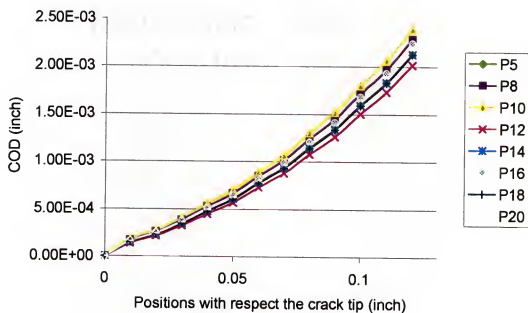
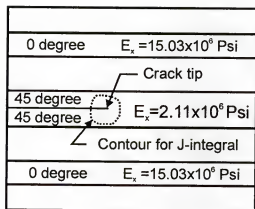
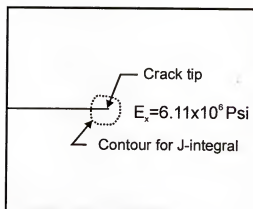


Figure 6-13. Crack opening displacement (COD) vs. positions (3D model)



3D Model, the Strain Energy is smaller around the contour



2D Model, the Strain Energy is bigger around the contour

Figure 6-14. Strain energy density of the 2D and the 3D model around the contour

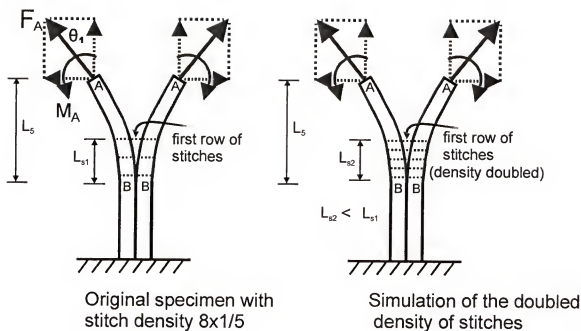


Figure 6-15. Simulation of the specimen with the twice stitch density

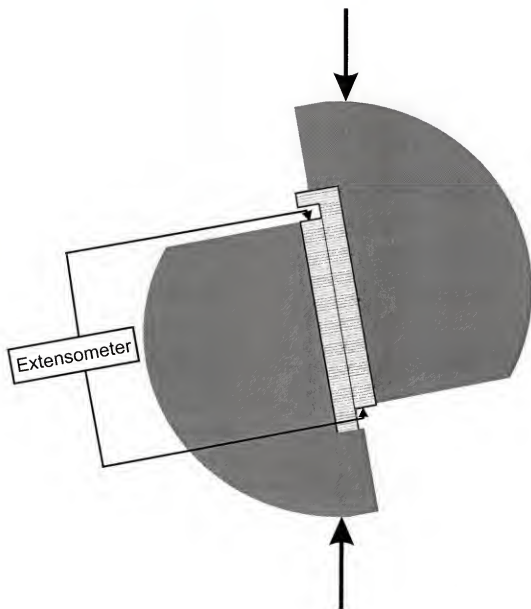


Figure 6-16. Novel shear test to determine the behavior of stitches under shear loading conditions.



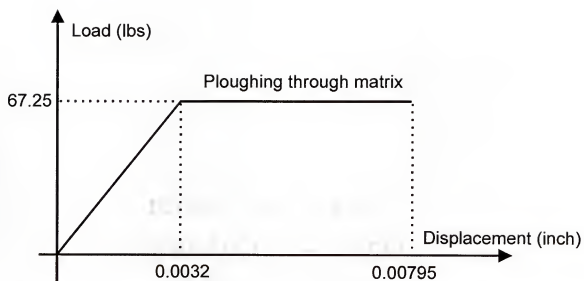


Figure 6-17. Model of stitch's behavior in Mode II

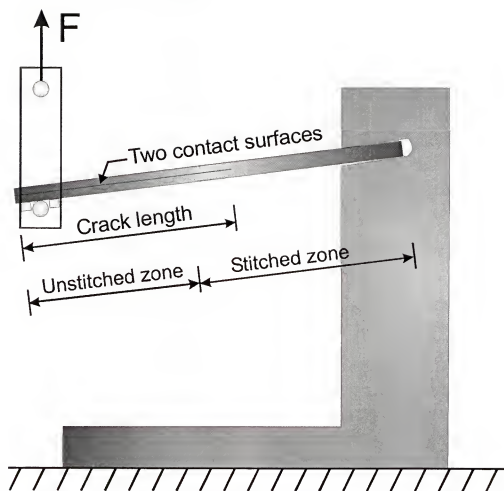


Figure 6-18. Setup for the mode II test.

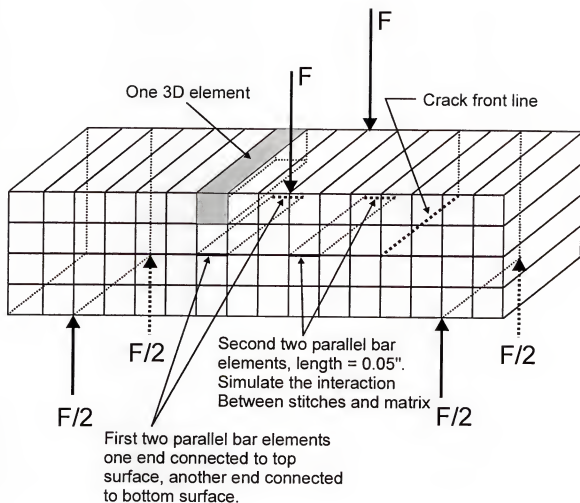


Figure 6-19. Schematic drawing of full 3D solid model for Mode II test (the actual mesh is much denser – the thickness of the element is equal to the thickness of each layer)

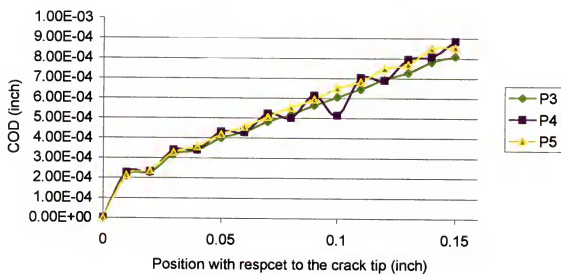


Figure 6-20. Crack opening displacement for Mode II under three different loading conditions

## CHAPTER 7 SUMMARY AND DISCUSSION

The standard DCB setup cannot be used to test the Mode I fracture toughness of composites with medium to high density stitches. Although fiber composites are strong in tension, their compressive strength is limited by fiber micro-buckling, which causes the specimens to fail before crack propagation. A novel Mode I test was developed to test the fracture toughness of stitched laminated composites. It can apply the extra tensile force required to neutralize the maximum compressive stress on the outer surfaces of a stitched specimen. Two analysis methods were developed to compute the instantaneous Mode I fracture toughness ( $G_{IC}$ ). One is for the preliminary loading fixture and  $G_{IC}$  can be calculated as  $\Delta W/(\Delta a \cdot b)$ . Another method utilizes an iterative method to solve the nonlinear governing equations to obtain the bending moment in the crack tip and  $G_{IC}$  can be obtained as  $M^2/(bEI)$ . The test method is versatile and easy to employ.

Two setups were used to obtain the Mode II fracture toughness of stitched laminated composites. In both setups, high sensitivity moiré technique was used to document the full displacement field as well as the exact position of the crack tip. Both setups show stable crack propagation due to stitching. In the Mode II test, the specimen undergoes large displacement and rotations making it difficult to apply high sensitivity moiré technique. The large carrier pattern should be

added to capture the displacement field around the crack tip. The moiré technique can be used to obtain the relative displacement between two crack surfaces, which is directly related to the stress intensity factor. When the position behind the crack tip is close to the crack tip, less than 0.01 inch (0.25 mm), the relative displacement can be used to calculate the  $K_{parent}$  (or  $G_{parent}$ ). However, as the position exceeds this range between 0.01 inch (0.25 mm) and 0.25 inch (6.4 mm), the relative displacement can be used to obtain the  $K_{eff}$  (or  $G_{eff}$ ). One should be careful when attempting to use this relationship to obtain the  $K_{eff}$  (or  $G_{eff}$ ) since these values vary with the location one selects. If one wants to obtain a fully developed bridging zone, the second setup is a better choice because it can provide a much longer crack length.

In Chapter 5, three new setups are used to test mixed Mode fracture toughness. Deficiencies of the first setup are that there was a limitation of the initial angles a specimen can be oriented (if the angle is too big, the specimen is going to break) and also the ratio of Mode I and Mode II is not constant during the test. It's difficult to identify the ratio of Mode I and Mode II since it changes during a test. For the second setup, the crack is unstable and ratio is almost fixed (there is a slight change of the ratio of Mode I and Mode II due to the axial forces although the contribution of the axial forces to  $G_{IC}$  is small). If one wants to obtain the instantaneous  $G^{mix}$ , the second setup is not good choice. The third setup is the best choice to test the mixed Mode fracture toughness for composites with the translaminar reinforcement. It has many advantages, for instance, the ratio is adjustable (one setup can be used to produce the pure

Mode I and pure Mode II and any conceivable ratio of Mode I and Mode II), the ratio changes little during a test (due to the unbalanced forces applied from the fixture, the specimen will tilt to one side and hence the ratio will change slightly during a test) and the fixture can be self-balanced to eliminate the error caused by the gravity of the fixture. Due to the lack of specimens, only two ratios of Mode I and Mode were tested by using the third setup. The author hopes in the future to test at least 6 to 10 different ratios using this fixture and then based on the experimental data, create a fracture criteria for composites with the translaminar reinforcement.

FEA models proposed in Chapter 6 provide valuable information about stitched composites. The potential of these models is to obtain accurate behavior of the stitches during the Mode I and Mode II tests. The behavior of stitches alone is totally different from that of stitches inside the parent materials. For the Mode I test, stitches are modeled as bar elements and stitches act like elastic material. They are connected to the top and bottom of the parent material. In reality, there exists the interaction between the matrix and the stitches and the strain and stress should vary throughout the length of a stitch. In order to more thoroughly understand the stitch's behavior inside the stitched composites, the author suggests using the new fixture described in Chapter 3 to pull out one or two stitches from the parent material. This test could shed light on the micromechanics of stitch failure. Then based on this test data, more accurate model of a stitch in Mode I can be established. In Chapter 6, only two simulations (doubling the density of the stitching and doubling the cross section

of a stitch) are used to determine the fracture toughness of stitched laminated composites. Many parameters can be simulated by using these models, for instance, changing the orientations of each layer, thickness of the specimen and even the properties of the parent material and stitches.

The behavior of stitches in Mode II is based on the new shear test (Figure 6-16). An extensometer is mounted on the specimen to document the relative displacements of the two crack surfaces. The load vs. displacement diagram was obtained after the two crack surfaces are separated (the stitches still connect the two separated surfaces). The stitch's behavior under Mode II loading is totally different from that under the Mode I loading. In Mode II test, stitches produce "shear forces" to prevent the two surfaces from sliding with each other. The stitches also cause local damage of the matrix. There is the friction between the two contact surfaces (they contact with each other before and after crack propagation). The coefficient of the friction may vary under various loading conditions. It's impossible to accurately model these effects. In our model, a "very short bar element" oriented along the two crack surfaces is used to simulate the behavior of a stitch in the Mode II test. This is not an exact model, however it certainly predicts the major behaviors of stitches in the Mode II test.



## REFERENCES

- [1] Mignery LA, Tan TM and Sun CT. "The use of stitching to suppress delamination in laminated composites," ASTM STP 876, American Society for Testing and Materials, Philadelphia, 1985, pp 371-385.
- [2] Dexter HB, Funk JG. "Impact resistance and interlaminar fracture toughness of through-the thickness reinforced graphite/epoxy," AIAA paper 86-1020-CP, 1986, pp 700-709.
- [3] Ogo Y. "The effect of stitching on in-plane and interlaminar properties of carbon-epoxy fabric laminates," CCM Report Number 87-17, Center for Composite Materials, University of Delaware, Newark, May 1987, pp 1-188.
- [4] Pelstring RM and Madan RC. "Stitching to improve damage tolerance of composites," 34th International SAMPE Symposium, May 1989, pp 1519-1528
- [5] Dransfield KA, Jain LK and Mai Y-W, "On the Effects of Stitching in CFRPS-I. Mode I Delamination Toughness," Composites Science and Technology, 58n, 6 June 1998, pp 815-827
- [6] Sharma SK and Sankar BV. "Effects of Through-the-Thickness Stitching on Impact and Interlaminar Fracture Properties of Textile Graphite/Epoxy Laminates," NASA Contractor Report 195042, February, 1995
- [7] Jain, LK and Mai Y-W "Mode I delamination toughness of laminated composites with through-thickness reinforcement," Applied composite Materials v1 n1 1994 pp1-17
- [8] Jain LK. "On the Effect of Stitching On Mode I Delamination Toughness of Laminated Composites," Composites Science and Technology, 51 1994, p 331-345
- [9] Jain, LK., Dransfield, KA. & Mai, Y-W. "Effect of Reinforcing Tabs on the Mode I Delamination Toughness of Stitched CFRPs," Journal of Composite Materials, Vol. 32, No. 22 (1998) pp 2016-2041
- [10] De Morais AB, De Moura MF, Marques AF and De Castro PT. "Mode-I interlaminar fracture of carbon-epoxy cross-ply composites," Composites Science and Technology v 62 n 5 April 2002 pp 679-686

- [11] Todo M and Jar P-YB. "Study of mode-I interlaminar crack growth in DCB specimens of fibre-reinforced composites," *Composites Science and Technology* v 58 n 1 Jan 1998. pp 105-118
- [12] Gong JC and Sankar BV. "Impact Properties of Three-Dimensional Braided Graphite/Epoxy Composites," *Journal of Composite Materials*, Vol. 25, June, 1991, pp 715-731.
- [13] Raris I and Poursartip A. "Delamination crack tip behavior at failure in composite laminates under mode I loading," *Journal of Thermoplastic composite Materials* v 11 n 1 Jan 1998. pp 57-69
- [14] Dickinson LC, Farley GL, and Hinders MK. "Translaminar Reinforced Composites: A Review," *Journal of Composites Technology & Research, JCTRE*, Vol. 21, No. 1, 1999, pp. 3-15.
- [15] Davies P, Blackman BRK and Brunner AJ "Standard Test Methods for Delamination Resistance of Composite Materials: Current Status," *Applied Composite Materials* v 5 n 6 Nov. 1998, pp 345-364
- [16] Choi NS. "Delamination Fracture of Multidirectional Carbon-Fiber/Epoxy Composites under Mode I, Mode II and Mixed-Mode I/II loading," *Journal of Composite Materials*, Vol. 33, No. 1/1999, 73-101
- [17] Dransfield K, Baillie C and Mai Y-W. "Improving the Delamination Resistance of CFRP by Stitching – a Review," *Composites Science and Technology* 50 (1994) 305 – 317
- [18] Brunner AJ "Experimental aspects of Mode I and Mode II fracture toughness of fibre-reinforced polymer-matrix composites," *Comput. Methods Appl. Mech. Engrg.* 185(2000) pp 161-172
- [19] Wu. E and Wang J. "Behavior of stitched laminates under in-plane tensile and transverse impact loading," *Journal of Composite Materials* v29 n17 1995 pp 2254-2279
- [20] Yum Y-J and You H "Pure mode I, II and mixed mode interlaminar fracture of graphite/epoxy composite materials," *Journal of Reinforced Plastics and Composites*, v 20 n 9 2001 pp 794-808.
- [21] Stevanovic D, Jar P-YB, Kalyanasundaram S and Lowe A. "On crack-initiation conditions for mode I and Mode II delamination testing of composite materials," *Composites Science and Technology*, v 60 n9 2000. pp 1879-1887

- [22] Chen L-S, Ifju PG, Sankar BV and Wallace B. "A Modified DCB Test for Composite Laminates with High-Density Stitches," Proceedings of the American Society For Composites, Fourteenth Technical Conference, Bethel, CT, Sept. 27-29, 1999, pp 214-217.
- [23] Chen L-S, Sankar BV, and Ifju PG. "A novel double cantilever beam test for stitched composite laminates", *Journal of Composite Materials*, 35(13) (2001)1137-1149.
- [24] Post, D, Han B and Ifju PG. "High sensitivity Moiré: Experimental Stress Analysis for Materials," Mechanical Engineering Series, Springer-Verlag, New York, NY (1994)
- [25] Jain, LK and Mai Y-W. "Determination of mode II delamination toughness of stitched laminated composites" *Composites Science and Technology* v 55 n3 1995 pp 241-253
- [26] Massabo R, Cox BN. "Concepts for Bridged Mode II Delamination Cracks", *Journal of the Mechanics and Physics of Solids*, 47 1999, pp 1265-1300.
- [27] Jain, L.K, Drandfield KA and Mai, Y-W "On the effects of stitching in CFRPs – II. Mode II delamination toughness", *composites Science and Technology* v 58 n 6 June 1998 pp 829-837
- [28] Clara S and Barry D.D "Evaluation of the accuracy of the four-point bend end-notched flexure test for mode II delamination toughness determination" *Composites Science and Technology* 60 (2000) 2137-2146.
- [29] Sih GC and Liebowitz H. "Mathematical Theories of Brittle Fracture" *Fracture and Advance Treatise (Volume II)* edited by H. Liebowitz (1968) Academic Press, New York and London
- [30] Ding, W. and Kortschot, MT. "Simplified beam analysis of the end notched flexure mode II delamination specimen," *Composite Structures* v 45 n 4 Aug. 1999. pp 271-278
- [31] Massabo R, Mumm DR and Cox BN. "Characterizing mode II delamination cracks in stitched composites" *International Journal of Fracture* 92, 1998 pp 1-38
- [32] Chen L-S, Sankar BV, and Ifju PG. "Mode II fracture toughness of stitched composites," *AIAA Paper 2001-1483, AIAA structures, Structural Dynamics & Materials Conference*, Seattle, Washington, April 2001

- [33] Jain, LK. and Mai Y. "Analysis of stitched laminated ENF specimens for interlaminar Mode II fracture toughness," *International Journal of Fracture* v 68 n 3 1994, pp 219-244
- [34] Ridards R and Korjakin A. "Interlaminar Fracture Toughness of GFRP Influenced by Fiber Surface Treatment," *Journal of Composite Materials*, Vol. 32, No. 17/1998, pp 1528-1559
- [35] Reeder JR. & Crews, JH Jr. "Mixed-mode bending method for delamination testing," *AIAA J* v 28 n7 Jul 1990, pp 1270-1276
- [36] Reeder JR and Crews JH Jr. "Redesign of the Mixed Mode Bending Delamination Test to Reduce Nonlinear Effects", *Journal Composites Technology and Research* (1992) pp 12-18
- [37] Shivakumar KN and Crews JH Jr. "Modified mixed-mode bending test apparatus for measuring delamination fracture toughness of laminated composites", *Journal of Composites Materials* v32 n9 1998 pp 804-828
- [38] Chen JH, Sernow R, Schulz E and Hinrichsen G. "Modification of the mixed-mode bending test apparatus", *Composites – Part A: Applied science and Manufacturing* v 30 n 7 1999 pp 871-877
- [39] Rugg KL, Cox B.N and Massabo R. "Mixed mode delamination of polymer composite laminates reinforced through the thickness by z-fibers," *Composites – Part A: Applied Science and Manufacturing*, v 33 n2 Feb. 2002 pp 177-190
- [40] Choi NS, Kinloch AJ and Williams JG. "Delamination Fracture of Multidirectional Carbon-Fiber/Epoxy Composites under Mode I, Mode II and Mixed-Mode I/II Loading," *Journal of Composite Materials*, Vol. 33, No. 1/1999, pp 73-100.
- [41] Ducept F, Gamby D and Davies P. "A mixed-mode failure criterion derived from tests on symmetric and asymmetric specimens" *Composites Science and Technology* 59 (1999) pp 609-619
- [42] Chen JH, Sernow R, Schulz E and Hinrichsen G. "A modification of the mixed-mode bending test apparatus" *Composites: Part A* 30 (1999) pp 871-877
- [43] Rikards R, Buchholz F-G, Wang H, Bledzki AK, Korjakin A and Richard H-A. "Investigation of mixed Mode I/II interlaminar fracture toughness of laminated composites by using a CTS type specimen," *Engineering Fracture Mechanics* 61 (1998) pp 325-342

- [44] Narayan SH and Beuth JL. "Designation of Mode Mix in orthotropic Composite delamination problems", *International Journal of Fracture* 90 (1998) pp 383-400
- [45] Bruno D and Greco F. "Mixed mode delamination in plates: a refined approach", *International Journal of Solids and Structures* 38 (2001) pp 9149-9177
- [46] Adeyemi NB, Shivakumar KN and Avva, VS. "Delamination fracture toughness of woven-fabric composites under mixed-mode loading", *AIAA Journal* v37 n4 April 1990. pp 517-520
- [47] Ifju PG, Chen L-S and Sankar BV. "Mixed Mode Fracture Toughness for stitched composites," SEM Annual Conference, Milwaukee, WI 2002 paper number 173.
- [48] Byun J, Gillespie JW and Chow T. "Mode I Delamination of A Three-Dimensional Fabric Composite," *Journal of Composite Material*, Vol. 24, May 1990, pp 497-518.
- [49] Chen VL, Wu, XX. and Sun CT. (1993) "Effective interlaminar fracture toughness in stitched laminates," *Proceedings of the 8<sup>th</sup> annual technical meeting of the*
- [50] Jain LK and Mai Y-W. "On the equivalence of stress intensity and energy approaches in bridging analysis" *Fatigue and Fracture of Engineering Materials & Structures* v17 n 3 March 1994 pp 339-350
- [51] Sankar BV and Zhu H. "Evaluation of failure criteria for fiber composites using finite element micromechanics" *Journal of Composite Materials* v32 n8 1998 pp 766-782
- [52] Sankar BV and Dharmapuri SM. "Analysis of a Stitched Doubled Cantilever Beam", *Journal of Composite Materials*, Vol. 32, No. 24/1998, pp 2203-2225
- [53] Rhee, KY and Lee H. "Two-term parameter technique to calculate energy release rate of composite laminates", *Composite Structures* v 42 n 2 June 1998 pp 169-174
- [54] Poursartip A and Chinatambi N. "Experimental determination of the Mode I behavior of a delamination under mixed-mode loading," *ASTM Special Technical Publication* n 1110, Published by ASTM, Philadelphia, PA, USA. pp 187-209

- [55] Sankar BV and Marrey RV "Analytical Method for Micromechanics of Textile Composites," *Composites Science and Technology*, 57 (1997), pp 703-713.
- [56] Sankar BV and Sonik V. "Modeling End-Notched Flexure Tests of Stitched Laminates," *Proceedings of the American Society for Composites Tenth Technical Conference*, Technomic Publishing Co., Lancaster, Pennsylvania, 1995, pp 172-181.
- [57] Sankar BV. (1991) "A Finite Element for Modeling Delaminations in Composite Beams", *Computers & Structures*, 38(2) pp 239-246.
- [58] Sankar BV and Dharmapuri SM "Analysis of a Stitched Double Cantilever Beam," *Journal of Composite Materials*, Vol. 32, No. 24/1998 pp 2203-2225
- [59] Renard J and Roudolff F. "Analytical and numerical calculation of strain energy release rate during delamination growth in a carbon epoxy laminate," *Composites Science & Technology*, v 42 n 4 1991 pp 305-316
- [60] Sankar BV and Sonik V. (1995) "Pointwise Energy Release Rate in Delaminated Plates", *AIAA Journal*, 33(7) pp 1312-1318
- [61] Sankar BV and Sonik V. (1995) "Modeling End Notched Flexure Test of Stitched composite Laminates" *Proceeding of the American Society for Composites, Tenth Technical Conference*, Technomic Publications, Lancaster, Pennsylvania, pp 172-181
- [62] ABAQUS Standard User's Manual (Version 6.2), Hibbitt, Karlsson & Sorensen, Inc. 2001
- [63] ABAQUS Theory Manual (Version 6.2), Hibbitt, Karlsson & Sorensen, Inc. 2001

## BIOGRAPHICAL SKETCH

Leishan Chen was born on March 9, 1963, in Jiangsu province, China, as the youngest child of Decun Chen and Shanyue Meng. He has two sisters, Xiaolan Chen and Lirong Chen. He graduated from Hohai University with a B.S. degree in Engineering Mechanics in July 1983. After graduation, he was a lecturer and a consultant in two colleges (Chang Jiang College and Zhe Jiang Shui Dian College) for more than 14 years. He married Dan Xie and has one son Rui Chen.

He came to the University of Florida for his graduate study in January 1998. He received his M.S. degree from the department of Aerospace Engineering, Mechanics and Engineering Science, University of Florida in 2000 and continued his Ph.D. study in the field of composites at the same department. He completed his Ph.D. program in August 2002.

I certify that I have read this study and that in my opinion it conforms to acceptable standards of scholarly presentation and is fully adequate, in scope and quality, as a dissertation for the degree of Doctor of Philosophy.



---

Peter G. Ifju, Chair  
Associate Professor of Aerospace,  
Engineering, Mechanics, and Engineering  
Science

I certify that I have read this study and that in my opinion it conforms to acceptable standards of scholarly presentation and is fully adequate, in scope and quality, as a dissertation for the degree of Doctor of Philosophy.



---

Bhavani V. Sankar, Cochair  
Professor of Aerospace, Engineering,  
Mechanics, and Engineering Science

I certify that I have read this study and that in my opinion it conforms to acceptable standards of scholarly presentation and is fully adequate, in scope and quality, as a dissertation for the degree of Doctor of Philosophy.

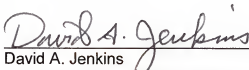


---

Nicolae D. Cristescu  
Graduate Research Professor of Aerospace,  
Engineering, Mechanics, and Engineering  
Science

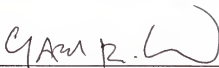


I certify that I have read this study and that in my opinion it conforms to acceptable standards of scholarly presentation and is fully adequate, in scope and quality, as a dissertation for the degree of Doctor of Philosophy.



David A. Jenkins  
Associate Engineer of Aerospace,  
Engineering, Mechanics, and Engineering  
Science

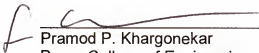
I certify that I have read this study and that in my opinion it conforms to acceptable standards of scholarly presentation and is fully adequate, in scope and quality, as a dissertation for the degree of Doctor of Philosophy.



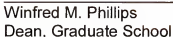
Gary D. Consolazio  
Assistant Professor of Civil and Coastal  
Engineering

This dissertation was submitted to the Graduate Faculty of the College of Engineering and to the Graduate School and was accepted as partial fulfillment of the requirements for the degree of Doctor of Philosophy.

August 2002



Pramod P. Khargonekar  
Dean, College of Engineering



Winfred M. Phillips  
Dean, Graduate School